



PONTIFICIA UNIVERSIDAD CATOLICA DE CHILE  
FACULTAD DE FISICA  
DEPARTAMENTO DE FISICA

**Individual Breast dosimetry for  
mammographic exams:  
a back-projection approach**

por

CAMILA BELEN RIOSECO MORA

Tesis presentada a la Facultad de Física de la  
Pontificia Universidad Católica de Chile  
para obtener el grado académico de Magíster en Física Médica.

Supervisores: Dra. Beatriz Sánchez (PUC Chile)  
Dr. Edgardo Dörner (PUC Chile)  
Dr. Peter Häring (Universidad de Heidelberg)

2017  
Santiago, Chile.

Medical Faculty Heidelberg  
Ruprecht-Karls-University Heidelberg

Master's Thesis  
"Clinical Medical Physics"

submitted by  
Camila Rioseco Mora

born in Santiago, Chile

2017

Individual Breast dosimetry for mammographic exams:

a back-projection approach

This Master's thesis has been composed by

Camila Rioseco Mora

at

Pontificia Universidad Católica de Chile

under the supervision of

Prof. Beatriz Sánchez Nieto, PhD

Pontificia Universidad Católica de Chile

Prof. Edgardo Dörner Yaksic, PhD

Pontificia Universidad Católica de Chile

and

Prof. Peter Häring, PhD

Heidelberg University

Individual Breast dosimetry for mammographic exams: a back-projection approach.

#### ABSTRACT:

The aim of this project is to propose and validate a procedure for estimating a dose at the axial plane of the breast in patients under mammographic exposure by means of electronic portal imaging device (EPID) dosimetry.

In vivo transit dosimetry consists of measuring the transmitted radiation through the breast with an EPID, and then back-projecting the fluence through the same volume in order to reconstruct the dose at a certain plane.

The methodology relies on the fact that from individual beam attenuation information, is possible to estimate dose deposition in the mammary gland.

Beam attenuation was calculated from the exit and entrance fluence.

Monte Carlo simulation of the entrance fluence was computed for three beam qualities. Exit fluence is calculated for each case, by deconvolution of the EPID image with previously determined composite kernel.

A complete model (i.e., X-ray tube, breast compression paddle, different breast thickness and detector) of the GE Senograph Essential with Tomosynthesis device, was simulated with EGSnrc. Specific codes as BEAMnrc and DOSXYZnrc were used for beam and detector simulations, respectively.

Three different beam qualities were simulated (only for 2D conventional mammography image acquisition) and additionally, and in-house graphical user interphase MATLAB<sup>1</sup> program “*BreDose*” was designed to estimate doses at an axial mid-plane of the breast from the EPID images.

---

<sup>1</sup> MATLAB version R2015b, academic use (May 18, 2015). The MathWorks, Inc.

Declaration:

I hereby certify, that I have composed the Master's Thesis independently, that no source materials or aids other than those mentioned have been used and that all citations have been declared appropriately.

Location, Date

---

Signature

# Contents

1 Introduction.....	1
2 Theoretical Framework.....	3
2.1 Mammography .....	3
2.2 Equipment and beam quality in mammography .....	3
2.2.1 X-ray tube characteristics .....	5
2.2.2 Beam Quality .....	9
2.2.3 Beam attenuation.....	10
2.3 Detectors in digital Mammography systems .....	14
2.3.1 Digital detectors .....	14
2.4 Mean Glandular Dose .....	17
2.5 EPID dosimetry .....	18
3 Hypothesis.....	21
3.1 Principal Objective .....	21
3.2 Secondary Objectives .....	21
4 Materials and Methods .....	22
4.1 Equipment.....	22
4.1.1 Mammogram unit.....	22
4.1.2 Dosimetric set.....	23
4.1.3 Images .....	24
4.1.4 HVL determination .....	26
4.1.5 Absorbed dose to water at the surface of the phantom.....	26
4.2 Monte Carlo simulation .....	29
4.2.1 Procedure to build the mammograph model .....	30
4.2.2 DOSXYZnrc and detector geometry.....	38
4.2.3 Data Base and Kernel generation .....	39
4.2.4 MC calibration.....	40
4.3 Kilovoltage backprojection model .....	42

4.3.1	Detector Calibration .....	44
4.3.2	Dose distribution at a mid-plane .....	45
5	Results.....	46
5.1	MC Spectral distribution.....	46
5.2	HVL .....	48
5.3	Heel effect.....	49
5.4	Kernels .....	50
5.5	Monte Carlo calibration factor .....	52
5.6	Detector Calibration factor .....	52
5.7	Deconvolved output fluence.....	53
5.7.1	Deconvolution process in Matlab.....	54
5.7.2	Validation of the deconvolution process .....	56
5.8	Absorbed dose at a mid-plane of the phantom.....	58
5.9	Mean Glandular Dose .....	61
5.10	Dosimetry tool “BreDose“.....	62
6	Discussion .....	65
6.1	MC validation .....	65
6.2	Kernel generation.....	66
6.3	MC calibration Factor .....	66
6.4	Detector calibration Factor.....	67
6.5	Deconvolution .....	67
6.6	Future work .....	68
Appendix A	.....	69
List of Abbreviations and Acronyms.....		69
Bibliography.....		70

To my son, Ismael.

## Acknowledgements

I would like to thank everyone at the Pontificia Universidad Católica de Chile and the University of Heidelberg who made it possible for this Master's program to fulfil the national and international requirements, as well as for allowing me to have participated in the program. I would especially like to thank my supervisors, Beatriz and Edgardo, for their supervision and answers to all of my questions during this process.

I would also like to thank Gabriela and Luis Fernando for dedicating their time and sharing their teachings with me, which were a great help for the completion of this work.

For their constant support, I would like to thank my friends Claudia, Isabella, Estefania, and Sol, who participated in my learning during this period.

For their unconditional love, understanding, and support of my son and me, I want to thank my parents Violeta and Enrique, as well as my life partner Matias, who has been with me at all times throughout this process.

Lastly, and most importantly, I would also like to thank my son Ismael, who has been the engine behind my projects since he entered my life, for his everlasting patience and his enormous love.

## 1 Introduction

*“Screening tests are used to find breast cancer before it causes any warning signs or symptoms.” “Breast cancer screening tests include clinical breast exam and mammography. For some women at higher risk of breast cancer, breast MRI may also be used.” [1]*

Mammography is an imaging technique used mostly to control and detect abnormal tissue in the breast. An early detection of abnormal tissue can prevent the development of breast cancer. However, image acquisition by mammography requires the use of radiation in the same way as conventional x-ray imaging. It has been established that the use of radiation, even at low doses, can induce the generation of secondary breast cancer by its accumulative effect [2]. It is important, then, to establish a trade-off between image quality and delivered dose to prevent undesired consequences.

The absorbed dose in the breast is highly dependent on the anatomy of it, which is therefore patient-specific. Additionally, the large heterogeneity of tissue composition in the breast makes it difficult to calculate an accurate dose deposition during image acquisition. One way to solve this drawback is by the calculation of a mean glandular dose which considers this heterogeneity.

Additionally, the resulting radiographic image after acquisition can be correlated with the total delivered dose. In radiotherapy treatments, for example, EPID images are used not only to control the dose distribution in the region of interest but also for determining the total delivered dose. It can be determined by the comparison between the fluence received from the detector and the fluence delivered by the head of the LINAC. In a similar approach, this comparison can be used in x-ray radiography equipment.

The purpose of this work is to show how to determine the delivered dose in a mammographic study and how to establish a trade-off between radiation and image quality. For this, it is necessary to introduce the physics related to X-ray tubes and the components of a mammography device (section 4.1). After that, a mathematical description about how to obtain the estimate the fluence from the detector is explained (section 4.3 and 5.7). It includes Monte Carlo (MC) simulations of the entire radiation path from X-ray tube emission to detection by the mammography detector (section 4.2). Results are presented in section 5.

## 2 Theoretical Framework

### 2.1 Mammography

Mammography is a radiographic examination designed to detect breast pathologies, particularly breast cancer [3]. The small X-ray attenuation differences between normal and cancerous tissues in the breast require the use of equipment specifically designed to optimize breast cancer detection [3]. Therefore, the mammographic system differs from the conventional X-ray equipment. Its distinctive parts are described in the following section.

### 2.2 Equipment and beam quality in mammography

The main challenge of the mammographic technique, is to generate an image of the breast with a sufficiently good quality in order to detect small cancerous lesions, while maintaining the radiation doses as low as possible.

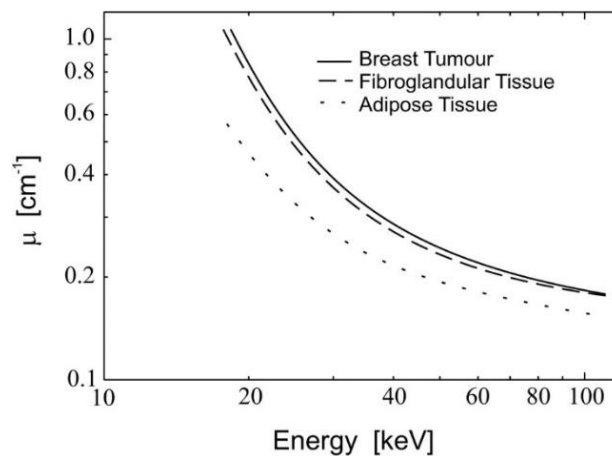


Figure 2-1 Attenuation of breast tissues as a function of energy, showing fat, glandular, and ductal carcinoma [4]

Figure 2-1 depicts the linear attenuation coefficients ( $\mu$ ) as a function of the X-ray energy, for: glandular, adipose and cancerous tissues. It is observed that the

differences between the three coefficients decrease with the energy of the X-rays. It is also noted that  $\mu$  values for glandular and cancerous tissues remain closer to each other along a large energy spectrum.

Tissues with different  $\mu$  values, are seen with different brightness in mammographic images, as tissues with higher  $\mu$  values absorb more rays passing through the breast, resulting in a lower intensity signal reaching the detector. By using low energy X-rays the contrast can be improved. However, low X-ray beams penetrate poorly through the breast, as they are absorbed more easily, producing poor signals at the detector leading to poor image qualities. A way of compensating for the poor signal while maintaining the contrast, is to increase the exposure times. As a consequence of this, the radiation doses delivered to the patient are increased. In general, mammography requires considerably longer exposure times compared to other radiographic procedures [5].

Mammography systems consist of specifically designed X-ray tubes alongside other essential elements such as a breast compression device (to reduce overlapping anatomy, decrease tissue thickness, and reduce inadvertent motion of the breast, among other benefits), antiscatter grids, X-ray detectors (screen-film or digital) and an Automatic Exposure Control system (AEC).

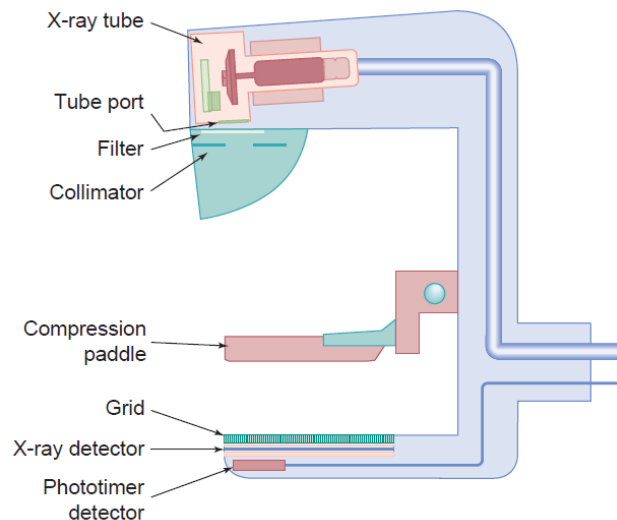


Figure 2-2 A given mammography system has many unique attributes. Major components of a typical system, excluding the generator and user console, are presented. [3]

Figure 2-2 contains the main components of a mammography system. It includes the X-ray tube, tube port, beam filter, collimator, compression paddle, anti-scatter grid, X-ray detector and phototimer detector.

### 2.2.1 X-ray tube characteristics

Within an X-ray tube, when current passes through the cathode (the filament), electrons are emitted from the filament by a process called thermionic emission [6]. These electrons are then accelerated by a potential of 50 *kVp*, or lower, towards the anode, where they transfer kinetic energy. Most of the interactions produce heat and no X-rays, but the majority of photons emitted due to Bremsstrahlung effect are usually generated with energies that are considerably lower than the *kVp*. These photons are most abundant at the low energies but range up to the *kVp* [7].

The mammography X-ray tube is configured with two filaments within the focusing cup in order to produce focal spots of different sizes (e.g., 0.1 – and 0.3 – *mm*). In general, the larger focal spots are used when images of the entire breast are needed (routine mammographies), whereas the smaller focal spots are used for magnified images of specific areas of the breast. X-ray tubes used for conventional radiographies use considerably larger focal spot sizes, usually in the range of 1.0– 1.2 *mm*.

The current of the filament is restricted (100 *mA* for large focal spots and to ~25 *mA* for small focal spots [3]) in order to control the amount of electrons reaching the target (anode) avoiding the overheating of the material. These current values limit the radiation doses to the glandular tissue while allowing good contrast and spatial resolution.

Molybdenum (Mo) were the most common anode target material used in mammography X-ray tubes. However, Rhodium (Rh) and Tungsten (W) are also used for thicker breasts. The characteristic radiation of Mo and Rh make them ideal materials as their K-shell characteristic radiation significantly increases the X-ray emission in the ideal energy range for mammography (for which highest contrast is

achieved) [3]. The K-shell for Mo are 17.5 and 19.6  $keV$ , and for Rh the K-shell energies are 20.2 and 22.7  $keV$  [3]

X-ray tubes can have rotating or stationary anodes in a block of copper, with an angle ranging from  $16^\circ$  to  $0^\circ$ , depending on the manufacturer. A tube with a  $0^\circ$  anode angle requires a tube tilt of about  $24^\circ$  to achieve an effective anode angle of  $24^\circ$ . A  $16^\circ$  anode angle requires a tube tilt of  $6^\circ$  for an effective angle of  $22^\circ$  [3]. This angle is responsible for the intensity of the X-ray beam to vary across the x-axis (left to right direction in Figure 2-3). The intensity is higher on the cathode side of the projected field and lower on the anode side. This effect is known as the *heel effect* [3] as depicted in Figure 2-3, and occurs due to the attenuation of the beam by the anode itself.

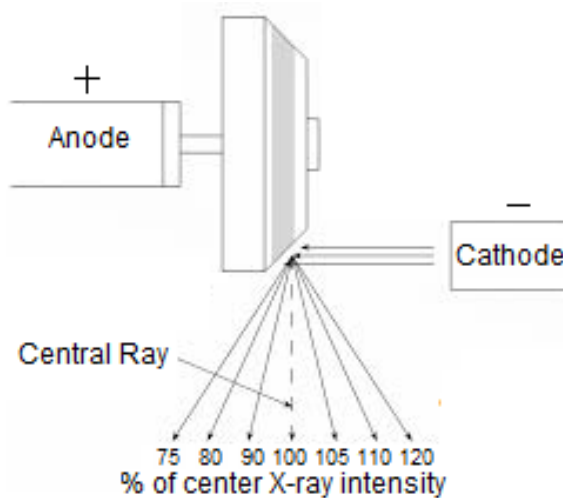


Figure 2-3 Anode heel effect [8]

### 2.2.1.1 Energy spectrum

The photon spectrum corresponds to the number of photons emitted per energy interval, as shown in Figure 2-4. The area under the curve represents the total number of emerging photons as described in the following equation:

$$\Phi = \int \frac{d\Phi E}{dE} dE$$

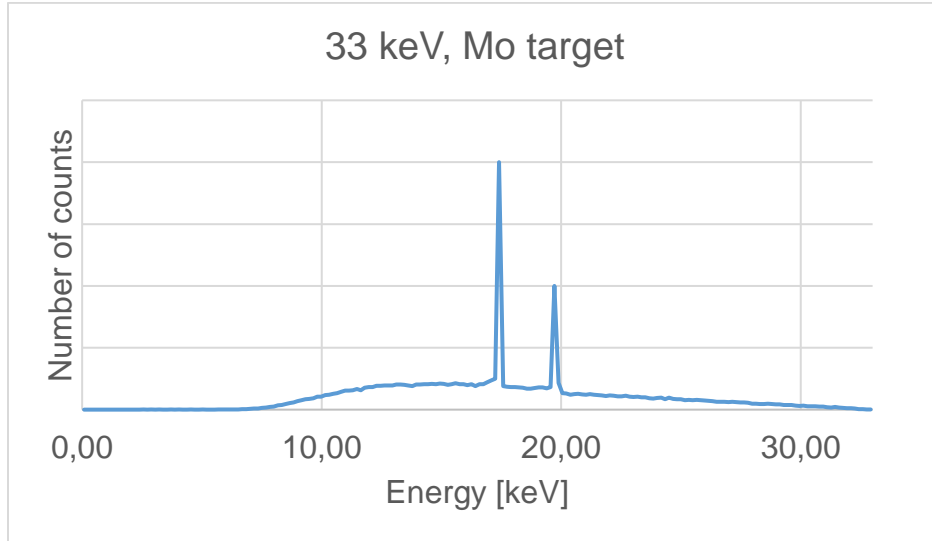


Figure 2-4 Spectral distribution of Mo, without filter at 33 kVp.

The spectral peaks represent the characteristic photons, and the continuous spectrum, ranging from 0 keV to 33 keV, represents the bremsstrahlung photons.

Several ways to characterize a beam of radiation exist, one of them is with the mean energy ( $\bar{E}$ ). To determine the mean energy, it is necessary to analyze the spectral distribution of a radiation field (particles or photons) described above, which is characterized by the fluence distribution or energy fluence with respect to energy.  $\Phi(E)$  is denoted as the photon fluence  $\Phi$  with energies between 0 and E. The differential distribution ( $\Phi_E$ ) of the fluence with respect to energy is given by:

$$\Phi_E = \frac{d\Phi(E)}{dE}$$

$\Phi_E dE$  is the photon fluence with energies between  $E$  and  $E + dE$ , thus, total fluence  $\Phi$  is:

$$\Phi(E) = \int_0^{E_{max}} \Phi_E dE$$

The mean energy ( $\bar{E}$ ) of a photon beam can be calculated as:

$$\bar{E} = \frac{\int_0^{E_{max}} \Phi_E E dE}{\int_0^{E_{max}} \Phi_E dE}$$

or,

$$\bar{E} = \frac{\int_0^{E_{max}} \Psi_E E dE}{\int_0^{E_{max}} \Psi_E dE} \quad (1)$$

if the mean energy is calculated from the distribution of energy fluence ( $\Psi_E$ ). Note that both expression of  $\bar{E}$  doesn't give the same value, so it is important specify the distribution used in the expression to obtain the mean value.

### 2.2.1.2 X-ray beam filtration

Once the X-Ray beam is generated at the target, the beam will be filtered by different materials in order to modify its energy spectrum.

The first inherent filtration is due to the exit window made of a very thin Beryllium layer. Regular glass is not used as it eliminates some of the desirable low energies. Additionally, some extra filtration is used to improve the distribution of the spectrum, removing some very low and high energies. Some of the most common combinations of target/filter are Mo/Mo, Mo/Rh, Rh/Rh [3]. As shown in Figure 2-5A, the Rh/Rh combination hardens the beam (with respect the Mo/Mo combination), which is better for thicker breasts, and removes the contribution of unwanted higher energies. Figure 2-5B, represents the Rh/Mo combination. It is seen that the Mo filter removes the second k-shell peak of Rh, which is useful for increasing contrast between mammary tissues. Therefore, the Rh/Mo combination is not useful.

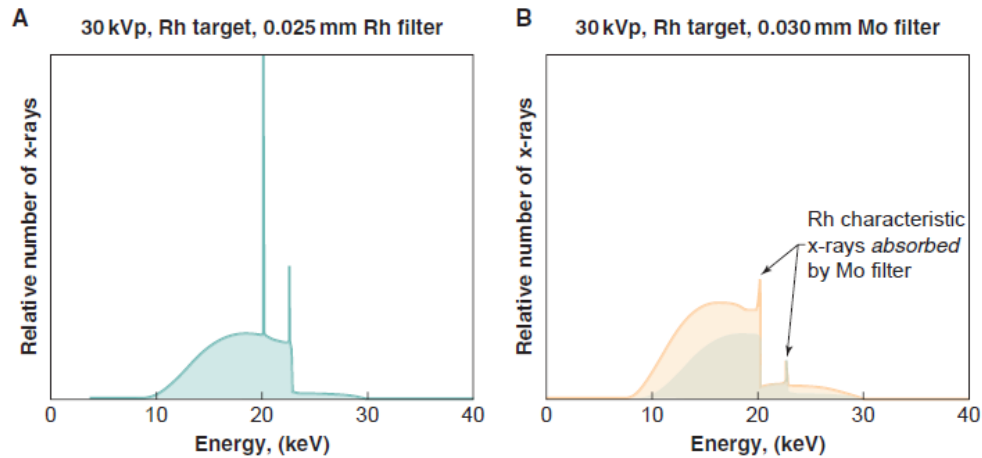


Figure 2-5 Two different spectrum of Rh target with Rh filter and Mo filter, and it is possible to see that the second configuration is not appropriate because the characteristic X-ray is strongly attenuated. [3]

### 2.2.1.3 Breast Compression

The compression paddle is an essential element of mammography systems and has various functions. First, it reduces the thickness of the breast, which leads to the reduction of exposure times and beam energy, as a less penetrating beam is needed, and as a result, delivered doses are reduced. Being allowed to reduce the beam energy also results in images with a better contrast, as well as in the reduction of the amount and effect of scattered radiation, which alters the geometric sharpness. Additionally, the compression paddle immobilizes the breast and movement unsharpness is reduced. It also reduces the amount of overlapping tissue and hence allows for a better visualization of internal structures.

### 2.2.2 Beam Quality

X-ray beam quality is characterized by its Half-Value Layer (*HVL*). *HVL* is the thickness of a material (usually Aluminum - Al) required to reduce by a one-half the initial intensity of the radiation. It depends on the target material (Mo, Rh, W), voltage (kV), filter material, and filter thickness. [3]

*HVL* value is obtained with the following equation:

$$HVL = \frac{t_2 \cdot \ln[2M_1/M_0] - t_1 \cdot \ln[2M_2/M_0]}{\ln[M_1/M_2]} \quad (2)$$

where  $t_1$  and  $t_2$  are the thicknesses of the filters used;  $M_0$  is the average value of readings without any added filter;  $M_1$  and  $M_2$  are the readings with different thickness of Al which are just above and below 50% of  $M_0$  respectively [9]. For mammography,  $t_1$  and  $t_2$  are usually expressed in mm and so HVL.

For mammography, *HVL* values range from 0.3 to 0.7mmAl for the *kV* range and combinations of target and filter material, according to the following equation [9]:

$$\frac{kV}{100} + 0.03 \leq HVL \leq \frac{kV}{100} + C \quad (3)$$

where *kV* is the measured value for nominal kV selected; and *C* depends on the different combinations [5]. For the target filter combinations of the beam quality simulated in this work, *C* values are presented in Table 2-1:

Table 2-1 *C* values according IAEA Quality Assurance Programme for Digital Mammography [9]

<i>C</i>		<i>HVL</i> values range, for different energies ( <i>E</i> ) used in this work	
Mo/Mo	0.12	$E = 26 \text{ kVp}$	$0.29 \leq HVL \leq 0.38$
Mo/Rh	0.19	$E = 29 \text{ kVp}$	$0.32 \leq HVL \leq 0.48$
		$E = 31 \text{ kVp}$	$0.34 \leq HVL \leq 0.50$

### 2.2.3 Beam attenuation

The attenuation of an X-ray beam in a medium occurs as a results of the interactions of photons with matter. In an ideal case, considering a monoenergetic parallel beam of intensity  $I_o$  reaching perpendicularly on a flat plate of material of thickness  $L$  (as shown in Figure 2-6), photons would be either absorbed completely or pass without interacting. In other words, no secondary radiation is produced.

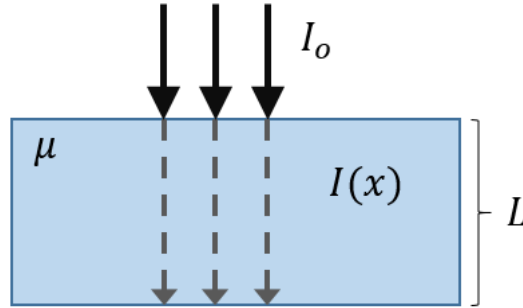


Figure 2-6 Diagram of a simple geometry of a photon beam traversing an object of thickness  $x$  and linear attenuation coefficient  $\mu$

If  $\mu$  is the probability that a particle interacts in a unit thickness of material traversed [10], the intensity of the beam after traversing a thickness  $x$  can be represented with the following exponential equation:

$$I(x) = I_0 e^{-\mu x} \quad (4)$$

Real beams are not ideal, and the interactions of the primary photons lead to the production of secondary radiation. That means, that the number of particles exiting the traversed material could be greater than the number of primary photons entering the material. If a detector is placed after the slab of material, it is important to know which particles should be counted in order to measure the attenuation of the material. If only the primary exiting particles are counted, and all the energy delivered to secondary particles is considered as absorbed, then the type of attenuation is considered to be a narrow-beam attenuation and an exponential behaviour is valid. If all particles reaching the detector are counted, then the amount of particles cannot be estimated using an exponential law, which is the case of a broad-beam attenuation [10].

The narrow-beam attenuation coefficient for a given medium will have a mean value  $\bar{\mu}$  that depends on the attenuator thickness  $L$  as well as on the detector response. For the case when the detector response is proportional to the incident

energy fluence (or the radiant energy), the mean narrow-beam attenuation coefficient  $\bar{\mu}_{\psi,L}$  observed at depth  $L$  is given by:

$$\bar{\mu}_{\psi,L} = \frac{\int_{E=0}^{E_{max}} \psi'_L(E) \mu_{E,Z} dE}{\int_{E=0}^{E_{max}} \psi'_L(E) dE} \quad (5)$$

where  $\psi'_L(E)$  is the differential energy-fluence spectrum through an attenuator of thickness  $L$ , and  $\mu_{E,Z}$  is the narrow-beam attenuation coefficient for energy  $E$  and atomic number  $Z$  [10].

In some cases, the mass absorption coefficient ( $\mu/\rho$ ), given by the quotient between the linear attenuation coefficient  $\mu$  and the density of the material  $\rho$ , is used instead. Both factors are published in NIST website [11] for many materials. In particular, for Polymethyl Methacrylate (PMMA), the behavior of  $\mu/\rho$  and values are presented in Figure 2-7 and Table 2-2:

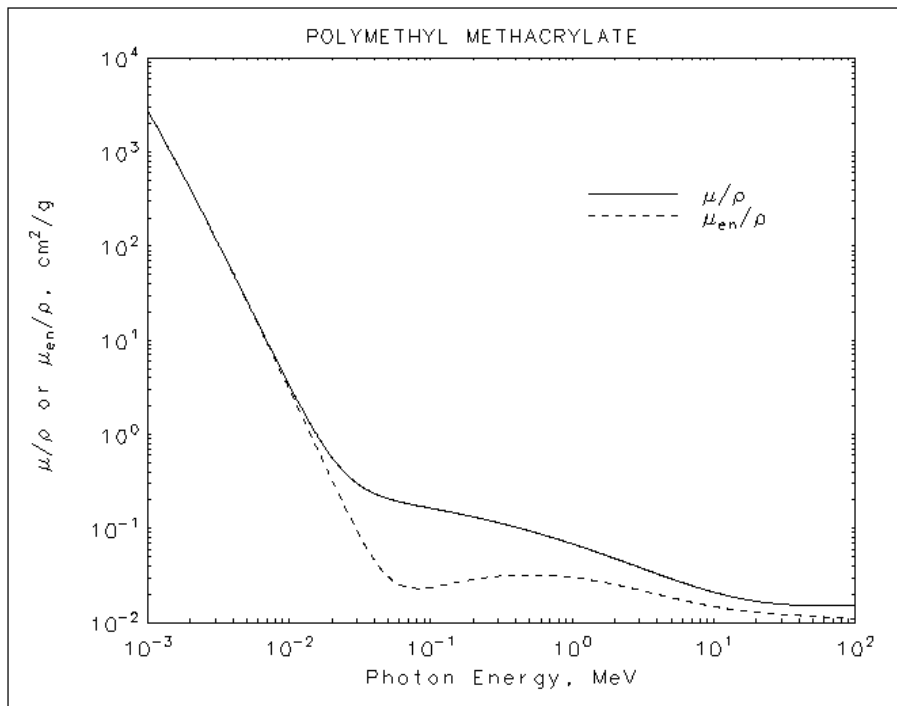


Figure 2-7 PMMA mass attenuation coefficient  $\mu/\rho$  and mass energy absorption coefficient  $\mu_{en}/\rho$  [11]

Table 2-2 Mass absorption coefficient for PMMA

Energy [keV]	$\mu/\rho$
1.0	2794.000
1.5	915.300
2.0	403.700
3.0	123.600
4.0	52.470
5.0	26.810
6.0	15.450
8.0	6.494
10.0	3.357
15.0	1.101
20.0	0.571
30.0	0.303
40.0	0.235

## 2.3 Detectors in digital Mammography systems

Detectors in digital mammography are designed to overcome several of the limitations inherent in the analog mammography system, and in so doing, potentially provides improved diagnostic image quality and a reduction of dose to the breast. Additionally, the benefit of digital mammography is to be able to use and manipulate the imaging in an immediate and effective way.

For the image formation, the detector interacts with the X-rays transmitted by the breast and absorbs the energy of the X-rays, converting this into a usable signal (generally light or electronic charge). Afterwards, it converts this signal into electronic charge (in the case of phosphor-based detectors). Finally, the detector system readout, amplified and digitalize the charge. [12]

### 2.3.1 Digital detectors

Digital detectors in mammography can be classified as indirect or direct. Indirect digital detectors absorb the X-rays and generates a light scintillation which posteriorly are detected by an array of photodiodes.

Direct digital detectors use a direct conversion method as the X-ray absorption and the creation of the electronical signal occurs in a single step.

The detector of the equipment simulated in this work is of the indirect type (with CsI as photostimulable material). However, the same geometry, can be used to simulate a direct detector, changing CsI by amorphous-Selenium (a-Se) as detection material.

#### 2.3.1.1 Indirect conversion detectors

Indirect conversion detectors are constructed in layers. Scintillator material converts X-rays into photons of visible light, usually cesium iodide doped with thallium (CsI: Tl). The second material used in indirect conversion detectors is amorphous-silicon (a-Si) which receives these beams and converts them into

electrical charge. These charges are then read with the panel transistor (TFT). Materials and processes are presented in Figure 2-8.

Lateral dispersion is generated by this process. To avoid this problem, the scintillator material is used as thin columns of few centimetres of diameter (approximately  $5\ \mu\text{m}$ ) and stacked laterally.

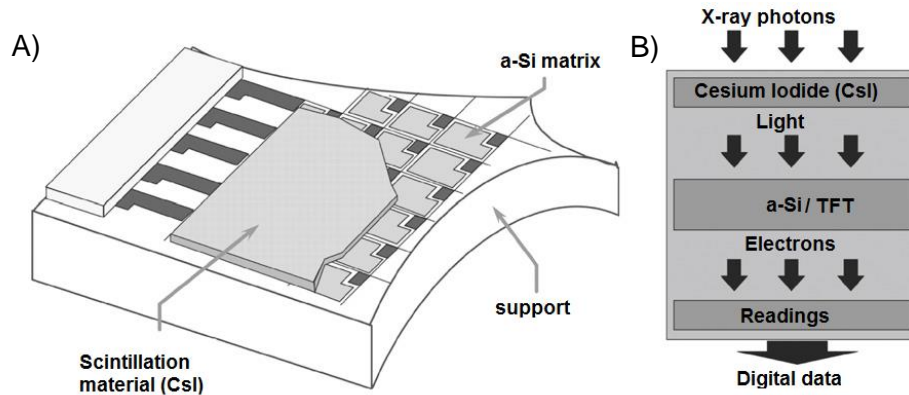


Figure 2-8A) Flat panel amorphous silicon with its fundamentals compounds and B) Schematic process of image acquisition in indirect conversion. [13]

### 2.3.1.2 Direct conversion detectors

Direct conversion detectors are made up of amorphous selenium (a-Se) material that interacts with the photons and produces a pair electron-hole. The electrons are then accelerated by a potential difference to different electrode plates, and with the TFT the charge is converted to signal. Figure 2-9 depicts an a-Se detector working scheme.

a-Se interacts highly at low X-rays energies as used in mammography. However, at high energies, that characteristic is inverted, due to a remanence charge that is necessary to delete before a new acquisition.

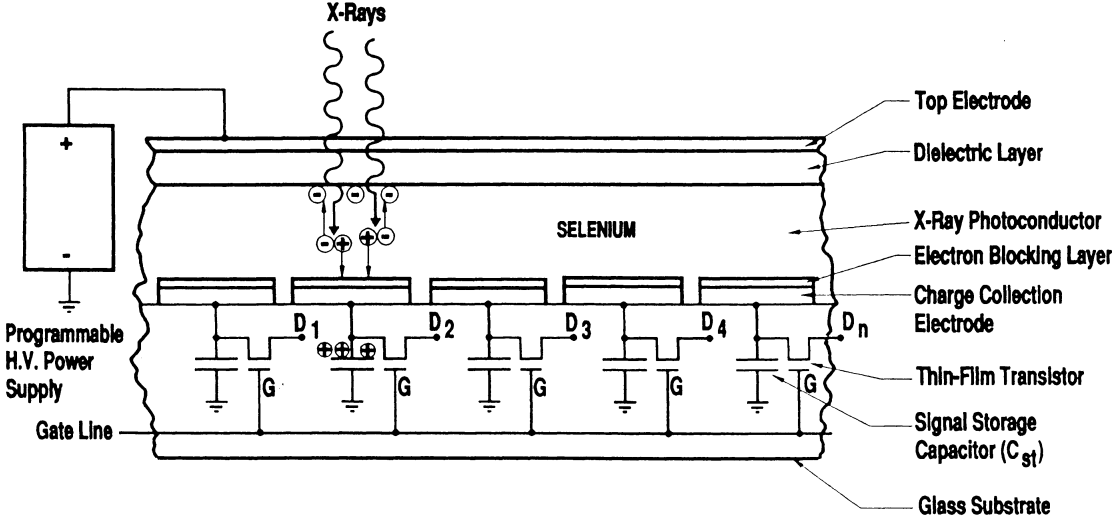


Figure 2-9 a-Se detector working scheme. [14]

## 2.4 Mean Glandular Dose

Ionizing radiation as used in low-dose X-ray mammography has been associated commonly with a risk of radiation-induced carcinogenesis. Pauwels et al. have recently published a study in which an estimation for the ratio of induced incidence rate over baseline incident rate of about 1.6% was found [15] for biennial screening.

The magnitude uses in mammography to quantify the absorbed dose to glandular tissue is *MGD*. The mean glandular dose (*MGD*) for a standard breast undergoing conventional mammography (2D) is calculated by the following equation [16]:

$$MGD = K \cdot g \cdot c \cdot s \quad (6)$$

where  $K$  is the incident air kerma at the top surface of the breast, measured without backscatter from the breast and  $g$  [17],  $c$  [18] and  $s$  [19] are conversion factors.

Achievable limits for mean glandular dose are between 0.6 – 5.1 *mGy*, depending on the thickness of the breast [9].

For breast dosimetry in tomosynthesis (3D), the formalism in equation (6) may be readily extended [16]. However, the simulation performed in this work corresponds to a conventional mammography.

Air kerma ( $K$ ) can be calculated with as follows:

$$K = M_{TP} \cdot N_{k,HVL} \quad (7)$$

where  $M_{TP}$  is the ion chamber reading corrected by pressure and temperature, and  $N_{k,HVL}$  is the in-air chamber calibration factor (in units of air kerma). This converts the chamber reading to air kerma under scatter-free conditions of the reference point of the chamber with the chamber assembly replaced by air (This calibration factor depends on the HVL).

## 2.5 EPID dosimetry

Electronic Portal Imaging Devices (EPIDs) were originally designed and used for patient setup during radiotherapy sessions. Nowadays, they are also used as tools for dosimetric evaluation, including dose delivery verification of intensity modulated radiotherapy treatments (IMRT). There are two approaches to EPID dosimetry: the “forward approach” and the “backward approach”. In the second one, portal images are used to reconstruct the dose within a patient or phantom. This back-projection method makes it possible to directly compare the calculated dose with the dose actually delivered to the patient or phantom [20].

Warkentin *et al.* [21] developed a convolution-based calibration procedure by using an amorphous silicon flat panel EPID for accurate dosimetric verification of IMRT treatments. In that model, raw EPID images were deconvolved to 2-D distributions of primary fluence using a scatter kernel composed of two elements: a Monte Carlo generated kernel describing dose deposition in the EPID phosphor, and an empirically derived kernel describing optical photon spreading.

Wendling, et al. [20] used the last back-projection algorithm and presented a back-projection EPID dosimetry method for two-dimensional IMRT dose verification. It was applied it to an amorphous silicon EPID, with a phantom in the beam. Most image acquisition systems process the images to improve the quality for setup purposes. However, this processing is not entirely useful for the dosimetric means. After the system acquires the images, they are processed with flood-field images (which correct for pixel sensitivity and non-flatness of the beam) and dark-field images (to eliminate electronic noise). The images obtained after these corrections are the ones stored by the system. For dosimetry purposes, the non-flatness of the beam has to be restored into the image. In this work, images are not processed, images used were “for-processing”, so they are not necessary be corrected.

For dose reconstruction, i.e., relating pixel values in the processed EPID images with absolute dose values in the phantom or patient, the characterisation of the following information is required: [20]

- a) the dose-response of the EPID;
- b) the lateral scatter within the EPID;
- c) the scattered radiation within the phantom or patient reading the EPID;
- d) the attenuation of the beam by the phantom or patient;
- e) the distance from the radiation source to the EPID plane and to the dose-reconstruction plane;
- f) the scatter within the phantom or patient to affect the reconstruction of the dose within the material.

The parameters for the back-projection algorithm were determined to enable the conversion from the dose at the EPID position to the dose inside the patient or phantom.

It is possible to express the dose at the position of  $i, j$  pixel of the detector ( $PD^{EPID}_{i,j}$ ) as follows:

$$PD^{EPID}_{i,j} = D^{EPID}_{i,j} \otimes^{-1} K^{EPID,1}_{i,j} \otimes K^{EPID,2}_{i,j} \quad (8)$$

where  $D^{EPID}_{i,j}$  is the dose value obtained from the pixel value according to the dose-response relation,  $K^{EPID,1}_{i,j}$  and  $K^{EPID,2}_{i,j}$  are EPID scatter correction kernels (in mathematical form),  $\otimes$  and  $\otimes^{-1}$  denote the convolution and deconvolution operator, respectively [20].  $K^{EPID,1}_{i,j}$  denote the kernel within the phantom and  $K^{EPID,2}_{i,j}$  denote dose deposition and glare within the detector.

It was concluded that this algorithm can accurately predict the dose in the midplane of a homogeneous slab phantom. [20]

In this work, a similar approach is proposed to estimate dose distributions after a mammographic exam. A backprojection model is proposed from low energy EPID images (between 20 kVp - 50kVp), deconvolved with kernels generated from Monte Carlo simulations. The equipment used and experimental setup are described in section 4.1, section 4.2 explains the simulations performed. Kilovoltage backprojection model, deconvolution model and MC validation are described in detail in section 4.3 and 5.7; **Error! No se encuentra el origen de la referencia..**

ose distribution at a mid-plane and finally an in-house develop dosimetry tool are described in section 4.3.2 and 5.10, respectively.

## 3 Hypothesis

The hypothesis of this project is that it is possible to determine the dose distribution at the axial mid-plane of the mammary gland by deconvolving images from the EPID detector after a mammographic exposure.

### 3.1 Principal Objective

Developing a kilovoltage backprojection tool for estimation of dose distribution on the mid-plane of one imaged breast.

### 3.2 Secondary Objectives

- 1) Generating a MC model of a digital mammogram equipment.
- 2) Generating a dose point kernel data base using MC for three beam qualities, each one with one breast thickness.
- 3) Proposing a dosimetric model for mammography based on EPID back-projection.
- 4) Implementing a tool for generating the dose distribution at a axial mid-plane of the mammary gland from the for-processing image [9].
- 5) Comparing the obtained planar dose distribution with the MGD value calculated.

## 4 Materials and Methods

### 4.1 Equipment

#### 4.1.1 Mammogram unit

The mammographic unit used in this study was a GE Senograph Essential with Tomosynthesis mammograph system (GE company, USA) (Figure 4-1) at the medical centre San Joaquín (Red de salud UC-Christus). Its Apollon X-ray tube, model number 5145113, operates with 22 to 49 *kV* range, 4 to 500 *mAs*; have two focal spot sizes: 0.1 and 0.3 mm; and a 0.69 mm beryllium inherent filtration. Also, the X-ray tube has two rotating anodes (Rhodium and Molybdenum) with different possibilities of added filtration: 0.03 mm of Mo and 0.05 mm of Rh. The source image distance (SID) used was 66 cm.

The equipment is used for the acquisition of tomosynthesis images, and standard 2D digital images. The tomosynthesis mode has a 25 degree angle scan with 9 projection images acquisition at 3.1 degree intervals. The exposure controls can be set using either of two modes: automatic or manual. The automatic mode uses the Automatic Optimization of Parameters (AOP), which selects the *kV*, *mAs*, and target / filter combination. In the manual mode, the operator chooses the parameters [22]. In this work, was use standard acquisition (2D digital mammography) in manual mode.

In this mammograph model, indirect conversion flat panel detectors are made of cesium iodine doped with thallium (CsI(Tl)) coupled with an amorphous silicon (a-Si). The system has 100  $\mu\text{m}$  pixel size and 24 × 30.7  $\text{cm}^2$  field of view. Thickness of the detector material (a-Si) is 250  $\mu\text{m}$ .



Figure 4-1 GE Senograph Essential with Tomosynthesis

#### 4.1.2 Dosimetric set

The ionization chamber is the most common device used to measure absorbed dose, kerma or exposure. It consists of a chamber with gas that is ionized by radiation. With an applied potential difference between the electrodes, the charge is collected. Under different factor corrections (due to the electronic measurement and environment) is possible to convert the value of the charge measured  $M$  in air kerma.

The ionization chambers used to measure kilovoltage X-rays in the low energy range are the parallel-plate chambers. Its entrance window is extremely thin in order to minimize the attenuation. The position of the chamber must be parallel to the beam direction.

It is crucial that the wall and body materials of the chamber have no significant energy dependence with low energy X-rays. [23]

A TN2334W PTW (PTW Freiburg GmbH company, Germany) parallel-plate ionization chamber (see Figure 4-2 A) was used for this study. It has a nominal sensitive volume of  $0.2 \text{ cm}^3$  and was designed to be used in low energy photon

beams ranging from 8 keV to 35 keV. An Iba electrometer, model Dose 1 (PTW Freiburg GmbH company, Germany) operate to +300 V, was used for this ionization chamber. (see Figure 4-2 B)

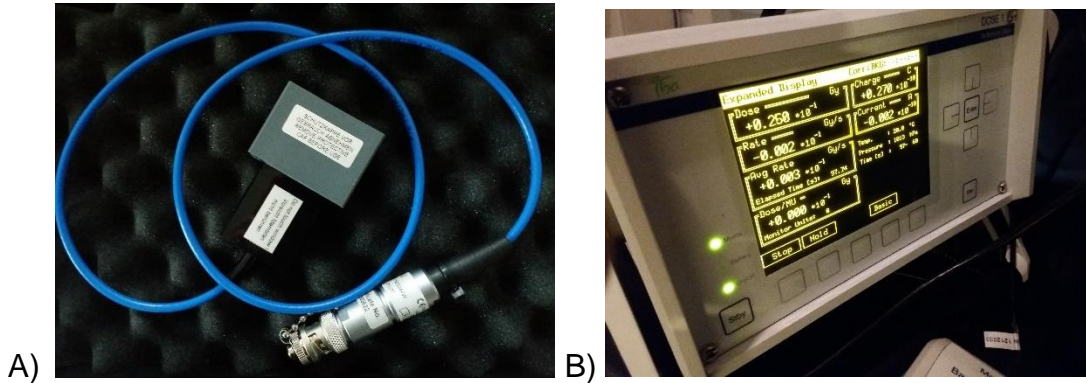


Figure 4-2 A) TN2334W PTW Parallel-plate chamber; B) Iba electrometer .

The dosimetric set (chamber + electrometer) was calibrated in terms of air kerma by the SSL University of Wisconsin-Madison laboratory for two beam qualities, presented in Table 4-1.

Table 4-1 Calibration factors provided by the secondary standard laboratory (SSD)

Beam quality	Air Kerma rate [mGy/s]	Air Kerma calibration coeff. [Gy/C]	Exposure calibration coeff. [R/C]	HVL mmAl
UW60-M	1.88	$7.600 \times 10^7$	$8.676 \times 10^9$	1.680
UW28-Mo	0.96	$7.917 \times 10^7$	$9.038 \times 10^9$	0.335

The  $N_k$  factor is used to convert the instrument reading at the beam quality concerned to air kerma free in air at the reference point. For any other beam user in the very low energy range can be estimated by interpolation of the factors, knowing the HVL of the beam.

### 4.1.3 Images

For the images that will be deconvolved, a PMMA phantom of  $19 \times 23 \text{ cm}^2$  (with slabs of 1 and 0.5 cm) was used, as seen in Figure 4-3.

Three different beam qualities were used to image the phantom (see Table 4-2)

Table 4-2 Thickness of phantom used for each beam quality

### **Configuration of the image acquisition**

1. Mo/Rh at 26 kVp, 50 mAs with 3.0 cm of phantom
2. Rh/Rh at 29 kVp, 63 mAs with 4.5 cm of phantom
3. Rh/Rh at 31 kVp, 71 mAs with 6.0 cm of phantom

One image was taken for each beam quality with an aluminum (Al) square ( $1 \times 1 \text{ cm}^2$ ) of 99,9% purity sandwiched in the middle of the PMMA phantom. The aluminum layer is positioned at 6 cm from anode side. This set up usually is used to obtain Signal Difference to Noise Ratio (SDNR) in detector performance, response and noise (see chapter 8.5 of Quality Assurance Programme for Digital Mammography, IAEA [9]). All images were used in order to obtain the detector calibration factor ( $C_{detector}$ ) (an input for the deconvolution, see section 4.3 for more details)



Figure 4-3 PMMA slab phantom placed in the mammograph for the depth dose measurement.

#### 4.1.4 HVL determination

HVL for Rh/Rh configuration operating at 29 kVp was determined. Four measurements of air Kerma were performed with the ionization chamber at 4.5 cm above the detector and compression paddle as close as possible from X-ray source to obtain *HVL* for one beam quality. The aluminum layers used in the measurements are listed in Table 4-3.

Table 4-3 Thickness of aluminum used for HVL determination.

	<b>Thickness of Al</b>
1.	0.0 mmAl
2.	0.2 mmAl
3.	0.4 mmAl
4.	0.5 mmAl

Each measurement was performed with the aluminum layers lying on the compressor paddle. This result was compared with the value calculated according to the IAEA protocol [9] (equation 4). Unfortunately, access restriction to the mammograph, avoided HVL measurements for the others two beam qualities (Mo/Rh 26kVp and Rh/Rh 31 kVp), so that these two *HVL* value were just estimated.

#### 4.1.5 Absorbed dose to water at the surface of the phantom

Dosimetry is the measurement of the absorbed dose to water, delivered by ionizing radiation. The expression to calculate the dose at the phantom surface for low energies photons (“X-rays generated at tube potentials lower than or equal to 100kV” [24])  $D_{\omega,z=0}$ , when the chamber is replaced by a phantom material, corresponding to the position of the front face of the chamber, is given by AIPEMB code of practice [25]:

$$D_{\omega,z=0} = M_{TP} \cdot N_{k,HVL} \cdot k_{ch} \cdot \left[ \left( \frac{\bar{\mu}_{en}}{\rho} \right)_{\omega/air} \right]_{z=0,\phi,HVL} \quad (9)$$

where  $M_{TP}$  is the instrument reading corrected by pressure and temperature,  $N_{k,HVL}$  is the calibration factor, and  $(\bar{\mu}_{en}/\rho)_{\omega/air}$  is the mass energy absorption coefficient

water to air ratio's average over the photon spectrum at the surface of the water phantom (values obtained from AAPM protocol [24]). The  $k_{ch}$  factor considers the change in response of the ionization chamber between the calibration in air and measurement at the surface of a full-scatter. Values are presented in Table 4-4 [25].

Table 4-4 The chamber correction factor ( $k_{ch}$ ) for PTW type M23344 chamber [25]

HVL (mm Al)	$k_{ch}$ values for PTW chamber types M23342 and M23344
0.04	1.01
0.06	1.01
0.10	1.01
0.12	1.02
0.15	1.02
0.20	1.03
0.30	1.03
0.40	1.04
0.50	1.05
0.60	1.06

The entrance dose ( $D_{\omega,z=0}$ ) has to be carried out with the ionization chamber. This chamber was used at the same position for all beam qualities due to the measurements were for a standard QA: at 6 cm from the chest wall edge placed, in air at 4.5 cm above the detector and with the compression paddle as close as possible to the ionization chamber [9]. Using the manual exposure mode, to define the desired kVp and mAs, the measurement is initially done. Three values for the current were used for each beam quality (see Table 4-5).

Each absorbed dose measured should be corrected by the inverse square law to get the entrance dose at the surface of each phantom (three different phantom thickness were used, not only 4.5 cm of thickness, and, as mentioned above, for each measurement, ionization chamber was placed in air at 4.5 cm above the detector)

*Table 4-5 Three beam qualities, each one with one thickness of PMMA above the detector.*

<b>Absorbed dose to water at the surface of the phantom</b>			
Target/Filter	Energy [kVp]	Current [mAs]	PMMA thickness [mm]
Mo/Rh	26	32	30
		40	
		50	
Rh/Rh	29	50	45
		63	
		71	
Rh/Rh	31	63	60
		71	
		80	

## 4.2 Monte Carlo simulation

EGSnrc is a Monte Carlo platform written in MORTRAN, a FORTRAN preprocessor, which simulates the radiation transport of photons and electrons on matter for energies ranging from above a few keV up to several hundreds of GeV [26]. EGSnrc, BEAMnrc/DOSXYZnrc version 3 was used to simulate the mammograph. Simulations were calculated in a cluster, with 4 processors AMD Opteron 6380, 16C, 2.5/3.4GHz with OS Debian 8.0. Also, codes were compiled with GCC version 4.9.2-10.

EGSnrc includes two main user codes: BEAMnrc for modeling radiotherapy sources (which was developed as part of the OMEGA project to develop 3-D treatment planning for radiotherapy [27]), as well as the dose scoring and DOSXYZnrc for calculating dose distributions in a rectilinear voxel phantom [28].

BEAMnrc code was used to model the mammograph and, track all their particles from cathode to the top of the detector. In this way particles information (such the phase space) was obtained at the different levels of the geometry required for this investigation. At this stage, all parameters related to the specific geometry of each mammograph (combinations target/filter thicknesses each, focal point sizes, material and thickness of the compressor paddle, energy, distance source-detector) are defined, together with PMMA, breast tissue, water, etc., materials constituting the imaged phantoms.

To obtain dose deposition kernels, it is essential to get information about dose deposition on each voxel within the detector, for which the code DOSXYZnrc will be used. As an input for the DOSXYZnrc, the phase space of the beam before reaching the detector was used.

### 4.2.1 Procedure to build the mammograph model

In the following sections, geometric input parameters and materials for the simulations with BEAMnrc code as well as the phase space output files will be presented.

#### 4.2.1.1 Geometry

BEAMnrc requires information about components of the device, such as materials and dimensions, distance to reference plane and thickness of the GE Senographe Essential. These information and values were obtained from the headers of images generated by the mammograph equipment and the available literature [29] [30] [31].

The components to create the model were: X-ray tube, beryllium window, filter, collimator, air slab, compressor paddle, phantom, air gap and an ideal detector (see Figure 4-4). Table 4-6 shows all possible combinations of materials and dimensions to build the mammograph model with the same characteristics of the GE Senographe Essential.

Table 4-6 Material, thickness and distance from the top of the simulation of the different components. Also, each modular component used in simulation. Note that compression paddle and phantom need to match so that the thickness of the phantom modifies compression paddle coordinates.

X-ray tube	Modular component		XTUBE		
	Target	Material	Mo		Rh
		thickness (cm)	0,5		0,5
	Dimension	Start (cm)	-2.5		
		End (cm)	2.5		
	Degree		16		
	Focal Spot (cm)		0,03		
Be Window	Modular component		SALB		
	Characteristics	Material	Be		
		thickness (cm)	0.069		
	Dimension	Start (cm)	2.5		
		End (cm)	2.569		
Filter	Modular component		SALB		
	Characteristics	Material	Air	Mo	Rh
		thickness (cm)	0.003	0,003	0,005
	Dimension	Start (cm)	3.5		
		End (cm)	3.503		
Collimador	Modular component		BLOCK		
	Characteristics	Material	Pb		
		thickness (cm)	0.5		
	Dimension	Start (cm)	5.5		
End (cm)		6			
Paddle	Modular component		SALB		
	Compression paddle	Material	PMMA		
		thickness (cm)	0.3		
	Dimension	Start (cm)	59.7		
End (cm)		60			
Phantom	Modular component		BLOCK and SALB		
	Phantom Characteristics	Material	AIR	PMMA	Breast tissue
		thickness (cm)	6		
	Dimension	Start (cm)	60		
End (cm)		66			
Detector	Modular component		SALB		
	Phantom Characteristics	Material	AIR		
		thickness (cm)	1		
	Dimension	Start (cm)	66		
		End (cm)	67		
	Phantom Characteristics	Material	Cesium Iodide		
		thickness (cm)	0.025		
Dimension		Start (cm)	67		
	End (cm)	67.025			

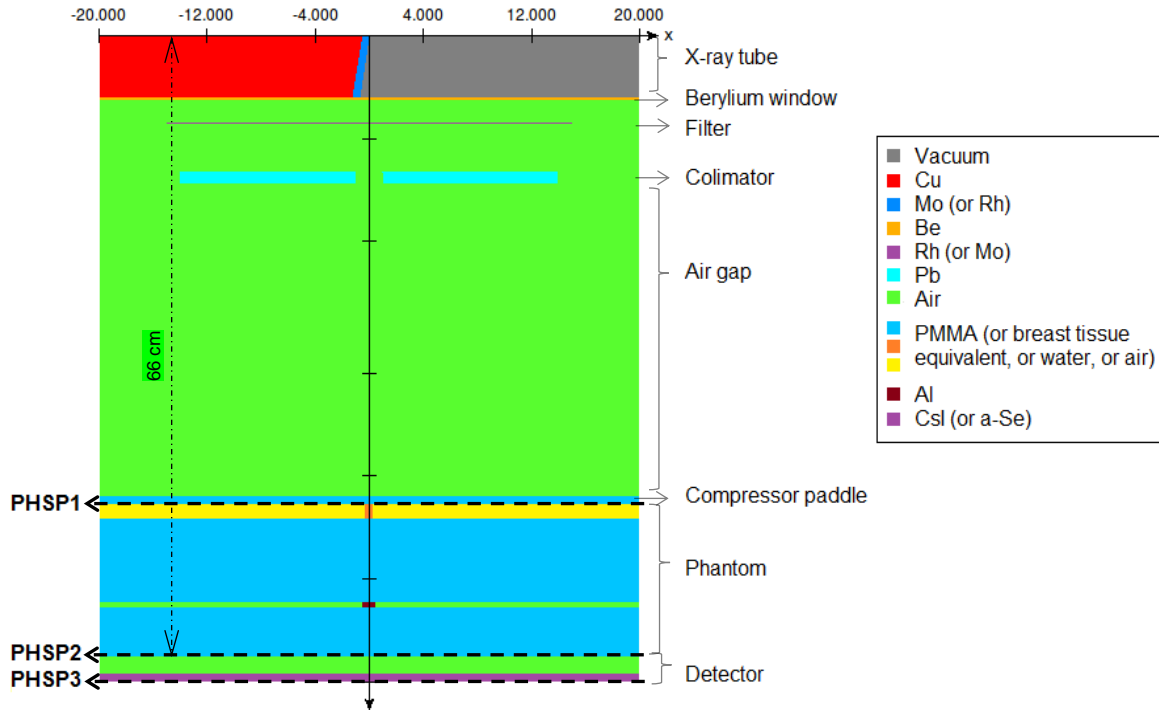


Figure 4-4 Mammograph components simulated in BEAMnrc. The diagram is not to scale. To visualize the phantom with their four components, three colors are presented in labels, but depicts PMMA material.

To simulate the mammograph, each component is characterized by a specific material, thickness, and distance from the top of the beam.

**X-Ray tube:** To generate the primary beam, it was initialized a parallel circular electron beam incident from the left side ( $0.0523\text{ cm}$  beam radius) to the Molybdenum (Mo) or Rhodium (Rh) target material, both with a thickness of  $0.5\text{ cm}$ . The material of region in front the target in the X-ray tube was vacuum and behind target was copper. The angle between target and z-axis was  $16^\circ$  to obtain  $0.3\text{ cm}$  of large focal spot. The thickness of the X-ray tube in z-direction is  $5\text{ cm}$ , and the distance of the front of material to reference plane was  $-2.5\text{ cm}$  to perform the incident beam in the central axis.

**Beryllium window:** The window where the radiation passes to the exterior of the X-ray tube is  $0.069\text{ cm}$  of beryllium.

**Filter** can be changed between  $0.003\text{ cm}$  of Mo or  $0.005\text{ cm}$  of Rh.

**Collimator:** This BLOCK has an aperture that allows a rectangular field on the top of the detector with  $24\text{ cm} \times 29\text{ cm}$ .

**Air slab:** In the case to get *HVL*, an air slab above the compression paddle was defined, to convert in aluminum layer with their specific characteristics (to perform experimental setup explained in section 4.1.4)

**Compressor paddle:** The distance from the top of the beam can be changed according to the thickness of the phantom below, to get a  $66\text{ cm}$  of SID.

**Phantom:** This should be of different materials: air, PMMA, breast tissue equivalent or liquid water. Phantom is divided in four parts to allow make changes according to the different necessities:

- I. Get entrance dose creating a virtual ionization chamber: This first part of the phantom is defined in the code as a BLOCK, with  $0.585\text{ cm}$  of thickness and diameter in the inner region, in order to create the ionization chamber volume (see section 234.1.2)
- II. Second part of the phantom is a SLAB who complete the distance between the first and third part of the phantom.
- III. In the real image, an aluminum layer was positioned between phantom plates, above  $2\text{ cm}$  of them, as explained in section 244.1.3. This third part of the phantom is defined as a BLOCK with an inner region with the same characteristics of the aluminum layer if the purpose of the simulation is compare images and obtained spectrum to create kernels. In the case of the *HVL* simulation, the inner and outer material of the BLOCK will be air.

This last part of the phantom is defined as a SLAB to complete the  $2\text{ cm}$  above the aluminum layer as the experimental setup.

**Ideal Detector:** Air gap corresponds to the distance between the breast/phantom and the image receptor, in this case was  $10\text{ mm}$ . The detector material used in the simulation was Cesium Iodine (CsI). Boone and Cooper [32] explain a methodology to validate the performance of a Monte Carlo simulation for

analysis of the scatter to primary radiation in the mammography setting. They compute and obtain experimentally the point spread function for a variety of physical variables as thickness, breast composition, for different air gaps between the breast and image receptor and different beam qualities. Sechopoulos et. al. [33] studied the behaviour of x-ray scatter in tomosynthesis by characterizing the scatter point spread functions and the scatter to primary ratio maps found in tomosynthesis with MC simulation considering the air gap between breast support and detector. Both studies recommend the air gap between 10 and 15mm depending on the energies and target combination. Montedoesca [31] used MC simulation to characterized scatter radiation in x-ray digital mammography and to validate the scatter point spread function with Sechopoulos et al. and Boone and Cooper, she used 10mm of AG obtaining a good agreement with the literature simulating the same beam qualities used in this work.

Interaction data for the materials used in this work, were obtained from PEGS4 (an EGSnrc platform), defined in the range of energies between 1 – 150 keV to get the interactions with the low energies simulated. Materials used were: copper, beryllium, molybdenum, rhodium, PMMA, breast tissue equivalent, air, aluminium, liquid water, cesium iodide (for indirect detection), amorphous selenium (for direct detection) (all these materials were obtained from Ghetti et al. [29])

Four beam qualities were simulated in this work, three of them are the described in Table 4-5 to compare with experimental data. Also, another beam quality of Mo target at 33 kVp without filter, was performed to analyse the heel effect.

#### *4.2.1.2 Monte Carlo Transport Parameter*

Other input data for the BEAMnrc are related with the cross-section data, optimization options of the simulation, number of histories, incident particle and source characteristics.

AE, AP are the maximum/minimum energies for which the data (cross section) of the materials are calculated (AE for secondary electron production (knock-on

electrons) and AP for bremsstrahlung production [34]). Then, due to the very low energy simulated in this work, the values of ECUT / PCUT, corresponding to the power cut for the transport of settled particles, are used. These values are listed in Table 4-7 I.

Simulation efficiency was increased with the directional bremsstrahlung splitting option using the parameters in Table 4-7 II. Directional Bremsstrahlung photon splitting (DBS) is one of the variance reduction techniques that improve the statistics of bremsstrahlung photons resulting from electron interactions. The philosophy of the technique is that bremsstrahlung photons aimed into a field of interest (encompassing the treatment field) are split at the time of creation, while those aimed away from the field are not [27]. DBS was used to improve the statistics of the particles at the surface of the detector since the very low energies particles are strongly attenuated through the beam. In this work, Bremsstrahlung splitting number was 10000 due to the statistics at the top of the detector.

All relevant processes at low energy are modelled, such as: Compton scattering, photoelectron angular sampling, Rayleigh scattering and atomic relaxations.

The number of histories (or particles) for all beam simulation was  $2 \times 10^9$  and the energy values varies between 26 – 31 keV depending on the experimental data.

*Table 4-7 MC parameters to initialize the beam*

BEAMnrc transport and reduction technique parameters	
I	<b>AE = Global ECUT</b> 0.512 MeV for electrons
	<b>AP = Global PCUT</b> 0.001 MeV for photons
	<b>Splitting field radius (cm)</b> 20
II	<b>Source to surface distance (cm)</b> 66
	<b>Bremsstrahlung splitting number</b> 10000

#### 4.2.1.3 Phase space output files and dose score

Binary phase-space files of the three beam qualities (Table 4-5) simulated at the end of the different planes (presented in Figure 4-4), were obtained with BEAMnrc.

- PHSP1 after the compressor paddle to get input fluence for the breast or phantom;
- PHSP2 after the phantom material to create a pencil beam kernel according to the spectrum;
- PHSP3 after the CsI, to compare MC output fluence with the image generated at the detector, to get a detector calibration factor (see Section 4.3.1)

A dose score region ( $0.2 \text{ cm}^3$ ) was defined at the upper portion of the phantom to estimate MC entrance dose ( $D_{entrance}^{MC}$ ).

To analyze a phase space data file for different purposes (derive fluence versus position, energy fluence versus position, spectral distribution, energy fluence distribution) it is necessary to work with the BEAMdp program [35].

To obtain input fluence at the breast entrance and output fluence at the detector exit, five regions of interest in PHSP1 and PHSP3 were selected to get the fluence per position (or ROI), called 1, 2, 3, 4 and 5, with BEAMdp code. Each one is  $1 \times 1 \text{ cm}^2$  and the distance between each region is  $0.5 \text{ cm}$ .

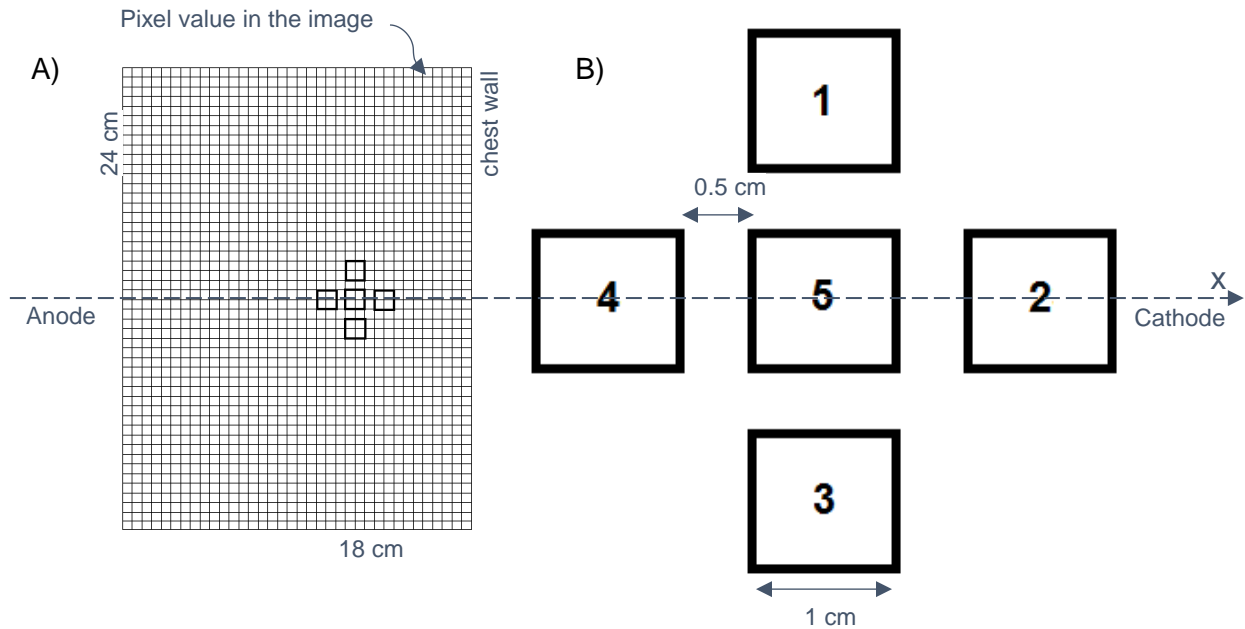


Figure 4-5 Scheme of the ROIs selected. Figure A shown a scheme of an image, each square represents a pixel value and ROI5 is positioned 6 cm from the chest wall in the central axis. Figure B depicts regions of interest. In the case of the phase space files, ROI 5 is positioned at the central axis.

Fluence of phase space 3 is compared with the image generated at the detector. Region 5 coincides with the same position where was positioned the aluminum layer as explained in section 4.1.3.

*In the case of the phase space files, region 5 of*

Figure 4-5B coincides with the axis of the beam, ROIs 4, 5 and 2 are along the x-axis (anode-cathode) and ROIs 1, 5 and 3 are along the y-axis.

#### 4.2.1.4 Heel effect

Before generating the pencil beam kernel for the three combination mentioned in Table 4-5, is necessary to understand how the spectral distribution varies along the X-axis (anode - cathode direction), where heel effect exists (explained in section 2.2.1). Five regions along the x-axis profile, of a reference beam quality of Mo target at 26 kVp without filter (field size of  $24 \times 19 \text{ cm}^2$ ), were study in order to verify that they are unaffected by the effect mentioned above.

The spectrum of 5 regions of  $1 \times 1 \text{ cm}^2$  along the x-axis of the beam, were chosen as described in Table 4-8:

Table 4-8 Distance of each region in the x-axis profile

Region	Distance of the x-axis profile
1	-12 cm to -11 cm
2	- 6 cm to -5 cm
3	- 0.5 cm to +0.5 cm
4	+5 cm to +6 cm
5	+11 cm to +12 cm

Intensities of these regions and the total energy were estimated and normalized to the central region (region 3).

#### 4.2.1.5 Generation of Pencil Beam Kernel

In order to generate the spectrum to create the pencil beam kernels within the detector, the spectrum of the central ROI ( $1 \times 1 \text{ cm}^2$ ) of each beam quality lists in Table 4-5 be obtained from the PHSP2 using BEAMdp program (wich generates the spectrums).

The result of BEAMdp was edited to convert these files into a new file, whose extension should be ".spectra" as required by the DOSXYZnrc code.

#### 4.2.2 DOSXYZnrc and detector geometry

To understand the detector response, it is necessary know these main parameters, such as the distance from source to active material, material, distance of the pixel in the z-axis, pixel size, number of pixels in different axis (x and y), and the medium where detector is within (to estimate the back-projection of the radiation).

To achieve deposition kernel into the detector, we made a small detector with real physical dimensions. Simulations were performed with  $0.31 \times 0.31 \text{ cm}^2$  square

dimension of Cesium Iodide (CsI), 0.01 *cm* pixel size (100 $\mu$ m), 31x 31 number of pixels in x-axis and y-axis. The pixel size in z-axis was 0.025 *cm* thickness, and they were divided into 25 values of pixel to view the deposition dose. Detector material was placed 1 *cm* below air gap (AG), according to the recommendations [32].

It is possible to use different beams for the interaction with the phantom, including the phase space that the BEAMnrc gives in the output, or spectra files. The input of the detector was spectra files created before with the second phase space (PHSP2). The number of histories was  $2 \times 10^8$  particles.

### 4.2.3 Data Base and Kernel generation

Three phase spaces are obtained from the BEAMnrc simulation (for each beam quality, breast size and target / filter combination), the first one, PHSP1, gives the input fluence to the breast, whose information will be relevant in order to know how much the beam is attenuated when traversed through the material. The third phase space, PHSP3, gives us the output fluence information of the scintillator material, which information will be compared with the EPID image of the detector to obtain the detector calibration factor (see Section 4.3.1 for more details)

Output data obtained from DOSXYZnrc is a “3ddose” file, which contains six rows with the information about the simulation geometry and the dose distribution with their uncertainties. Row five contains dose values of the detector geometry (in  $n_x n_y n_z$  format) these values are used to create a 3D matrix in Matlab with the same dimensions of the detector.

A database containing 4 files with the following information was generated:

- The number of photons arriving in each region defined in Figure 4, for each of the phase spaces mentioned before (PHSP1 and PHP2, for each of the simulated beam qualities)
- The dose deposited in the detector. That file has one single row with the information of the dose with  $n_x n_y n_z$  values

- the experimental entrance dose to compare with the MC entrance dose to calibrate each simulation (see Section 4.2.4 for more details)

#### 4.2.4 MC calibration

The primary beam simulated in this work was an electron beam incident on the target. The number of particles or the number of histories ( $NH$ ) and affect the statistics of the simulation. However, in a real X-ray tube, the number of particles hitting the target depends on the tube current and on the potential difference between anode-cathode, affecting the number of photons generated and thus, the fluence and dose. It is necessary calculate a factor who carries the correspondence between the dose deposited per tube current and the number of histories needed to generate the same dose.

When entering the values of the simulation parameters, the region where the dose is to be measured is indicated. In this way, the zone of "ionization chamber" was defined with the same sensitive volume of  $0.2 \text{ cm}^3$  and the dose is stored in that region. The information of this value is found in an *egs/st* file containing information of the geometry, total number of particles incident per plane and the dose per region.

To calibrate MC simulations, a calibration factor  $C_{MC}$  will be obtained from the comparisons between experimental entrance dose ( $TC D_{entrance}^{exp}$ ) and MC entrance dose ( $D_{entrance}^{MC}$ ):

$$C_{MC} = \frac{TC D_{entrance}^{exp}}{D_{entrance}^{MC}}$$

where  $TC$  is the value for each tube current value.

However, experimental entrance dose varies depending on the tube current ( $TC_i^{exp}$ ) used (at higher tube current value, higher number of electrons impact the target, fluence is increased and, therefore, the dose), so it is necessary normalize by this value for measure  $i$ :

$${}_{TC_i}^N D_{entrance}^{exp} = \frac{TC D_{entrance}^{exp}}{TC_i^{exp}} \left[ \frac{Gy}{mAs} \right]$$

now, the experimental entrance dose is independent of the number of photons generated in the target and should be the same for all beam qualities measured.

On the other hand, MC entrance dose given as a dose deposited by particle so that it is possible to calculate the total dose deposited as follows:

$${}^{NH} D_{entrance}^{MC} = D_{entrance}^{MC} \times NH$$

where  $NH$  is the number of histories.

Finally,

$$\overline{C_{MC}} = \frac{1}{i} \sum_i \frac{{}_{TC_i}^N D_{entrance}^{exp}}{{}^{NH} D_{entrance}^{MC}} \left[ \frac{1}{mAs} \right] \quad (10)$$

where  $i$  is the number of  $TC$  used to get the mean value of  $C_{MC}$  for each beam quality.

Each data obtained with BEAMnrc, for each beam quality, must to be multiplied by this factor and tube current value.

### 4.3 Kilovoltage backprojection model

Knowing the entrance dose  $D_{entrance}^{exp}$  (i.e. the dose at the surface of the phantom, measured previously with ionization chamber), it is possible to calculate dose at any depth ( $D(z_{phantom})$ ) as follows:

$$D(z_{phantom}) = D_{entrance}^{exp} \cdot \left( \frac{SSD - d}{SSD - d + z_{phantom}} \right)^2 \cdot e^{-\bar{\mu}_M \cdot z_{phantom}} \cdot 100 \quad (11)$$

where  $z_{phantom}$  is the depth in the phantom for dose calculation,  $SSD$  is source surface distance,  $d$  correspond to the thickness of the phantom/breast,  $z_{phantom}$  is the depth of the point and  $\bar{\mu}_M$  is the mean value of the linear attenuation coefficient of the phantom or medium  $M$  between compression paddle and detector

It is possible to obtain  $\bar{\mu}_M$  value relating input and output fluence of the phantom with the following equation (as the same than the equation (2)):

$$\Phi_{out,(x,y)} = \Phi_{in,(x,y)} \cdot e^{-\bar{\mu}_M \cdot z_{phantom}}$$

$$\bar{\mu}_M = \frac{1}{d} \cdot \ln \left( \frac{\Phi_{in,(x,y)}}{\Phi_{out,(x,y)}} \right) \quad (12)$$

where  $\Phi_{in,(x,y)}$  and  $\Phi_{out,(x,y)}$  are input and output fluence respectively, in the position  $(x, y)$  as shown in Figure 4-6.

Several ways to obtain output fluence exists, one of them is by MC simulation; another one is by deconvolution of integrated electronic portal images (EPID) to obtain incident fluence into the detector, or phantom output fluence. Input fluence is obtained by MC simulation ( $\Phi_{in,(x,y)}^{MC}$ ) per beam quality and phantom thickness, that information is taken from PHSP1 explained in section 4.2.1.3.

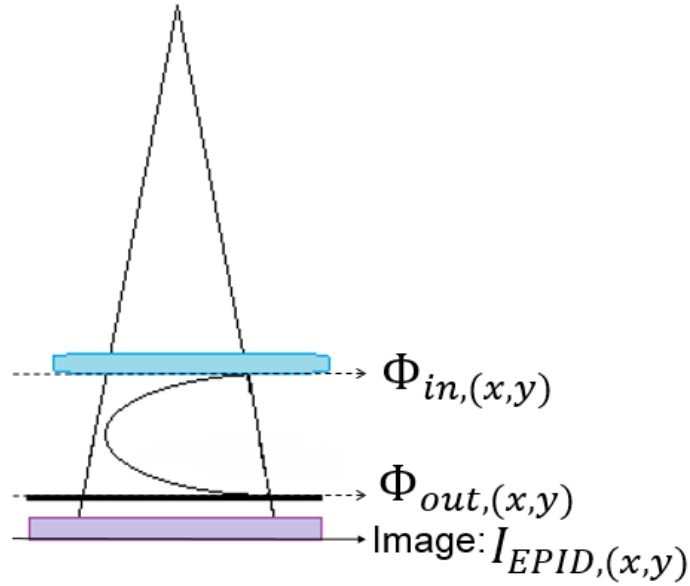


Figure 4-6 Scheme of the beam pass through the compression paddle (light blue), breast, carbon fiber (support of the breast, in black), air gap, and ideal detector of CsI

As the objective of this project is to develop an individual breast dosimetry, the output fluence is obtained by a deconvolution process and not by MC simulation due to the lack of information of each breast composition for the simulation. Effectively, the deconvolved output fluence ( $\Phi_{out,(x,y)}^{deconvolved}$ ) has the anatomy information of the breast. Therefore, it can be written that:

$$\bar{\mu}_M = \frac{1}{d} \cdot \ln \left( \frac{\Phi_{in,(x,y)}^{MC}}{\Phi_{out,(x,y)}^{deconvolved}} \right) \quad (12)$$

Note that  $\Phi_{in,(x,y)}^{MC}$  (from PHSP2) and  $\Phi_{out,(x,y)}^{deconvolved}$  (from image) are different because the detector efficiency.

Nevertheless, to characterize the detector efficiency, it is necessary to obtain MC output fluence ( $\Phi_{out,(x,y)}^{MC}$ ) obtained from PHSP2, but it will analyze in other section. The mean value of the linear attenuation coefficient of any medium between compressor paddle and detector is:

Deconvolution process uses images to obtain information of the breast, because of that, it is important understand that the radiation transport affects not only the dose within the breast, but also the quality of the detector. At low energies,

the predominant effects are photoelectric and scattering compton, especially in high Z value. This effect produces a decrease in the image contrast.

The parameters that affect the magnitude of scattered radiation include the X-ray spectrum, the compressed breast thickness, the breast composition, the size and shape of the field of view, the air gap between breast and detector, detector composition and thickness, grid characteristics, and the position of interest within the field of view [32].

The radiological images are created within the image receptor using the energy deposited from broth, primary and scattered photons. The primary photons have important information about different tissue within the breast, based on the differing attenuation of these tissues. Scatter or secondary photons are from different components of the mammograph. Therefore, by deconvolving the image with the deposition Kernel, the fluence at the entrance of the detector, after passing the breast, can be calculated (except for the correction factor for the detector efficiency)

#### 4.3.1 Detector Calibration

For our purposes, it is necessary to obtain the output radiation of the breast, which, from the conversion of gray values (produced due the interaction between photons and the material that converts them into electrical charge) to detector fluence values and subsequent deconvolution, we will get the output fluence of the breast, which will serve to know the dose in a plane of the breast, knowing the entrance fluence of the breast.

To convert gray values of the image ( $I_{EPID,(x,y)}$ ) obtained from the EPID to detector fluence values at the exit plane of the detector ( $\Phi_{det,(x,y)}$ ), another conversion factor is used ( $C_{detector}$ ), to incorporate detector efficiency (of electrons to photons conversion):

$$\Phi_{det,(x,y)} = C_{detector} \cdot I_{EPID,(x,y)} \quad (13)$$

The ratio of number of counts of five regions of interes (see

Figure 4-5),  $N_{MC}^{ROI_i}$  (from MC output fluence) and  $I_{EPID}^{ROI_i}$  (from image gray values) will give the calibration factor  $C_{detector}$  with the following equation:

$$C_{detector} = \frac{1}{5} \sum_{i=1}^5 \frac{N_{MC}^{ROI_i} \times TC \times \overline{C_{MC}}}{I_{EPID}^{ROI_i}} \quad (14)$$

The MC output fluence  $N_{MC}^{ROI_i}$  is obtained from PHSP3 file, which depicts the simulated output fluence (photons generated within Csl) at the end of the ideal detector. Calibration factor is obtained comparing simulated output fluence of photons with the signal (EPID image) according to the equation (15). Calibration factor has the information about the efficiency of the detector and others consideration as the idealization of this in the simulation. Note that the image is formed with the interactions of the electrons, thus  $C_{detector}$  has units of *[photons/electrons]*.

*Five regions of interest, explained in*

Figure 4-5, were analyzed from the EPID image and MC fluence. That was performed for each image obtained experimentally (see section 4.1.3). Detector calibration factor, for each beam quality, is the mean value of 5 factors obtained in 5 regions of interest.

### 4.3.2 Dose distribution at a mid-plane

As explained in section 4.2.3, in database contain a file indicating the input fluence of the breast, which will be standard for each combination, since the geometry of the beam path does not vary. In the same way, the input dose is calculated once for each combination.

Once the input fluence obtained in regions 1, 2, 3, 4, and 5 of

Figure 4-5 (and weighted by MC calibration) the linear attenuation coefficient is calculated with the deconvolution fluence data, for each region of interest according to the equation (12). Additionally, knowing all the parameters used in equation (11), the dose at any depth within the phantom.

## 5 Results

### 5.1 MC Spectral distribution

Spectra of the three beam qualities simulated (Mo/Rh at 26 kVp, Rh/Rh at 29 kVp and Rh/Rh at 31 kVp) are represented in Figure 5-1, Figure 5-2 and Figure 5-3 respectively. They resemble typical spectra for those target /filter configurations.

The first and second peak of the spectrum in the Figure 5-1 are located at energies  $17.475 \pm 0.025 \text{ keV}$  and  $19.575 \pm 0.021 \text{ keV}$  respectively. The power cut produced by the rhodium filter is  $23.475 \pm 0.258 \text{ keV}$ . In the Figure 5-2, peaks are located at energies  $20.18 \pm 0.02$  and  $22.73 \pm 0.03 \text{ keV}$  and the power cut produced by the rhodium filter is  $23.33 \pm 0.11 \text{ keV}$ . Figure 5-3 shows  $20.227 \pm 0.027 \text{ keV}$  and  $22.707 \pm 0.007 \text{ keV}$  peaks and the edge of the target equal to  $23.327 \pm 0.107 \text{ keV}$ . Table 5-1 contains all these values.

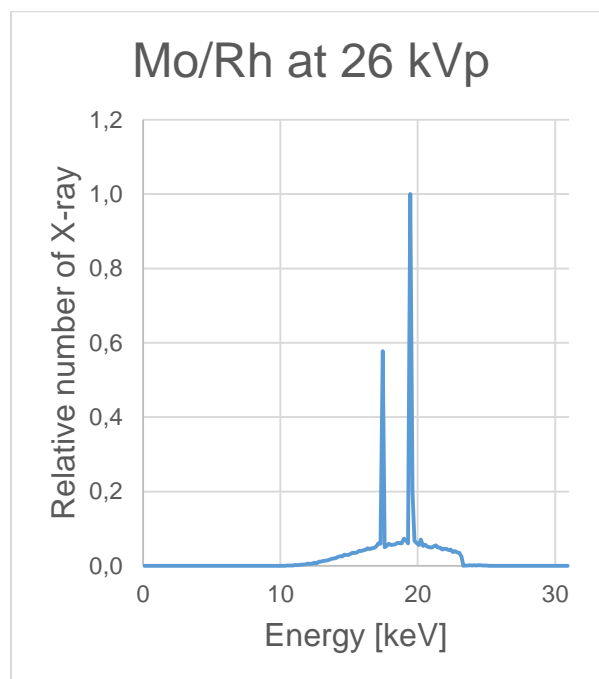


Figure 5-1 Spectral distribution of Mo/Rh at 26 kVp.

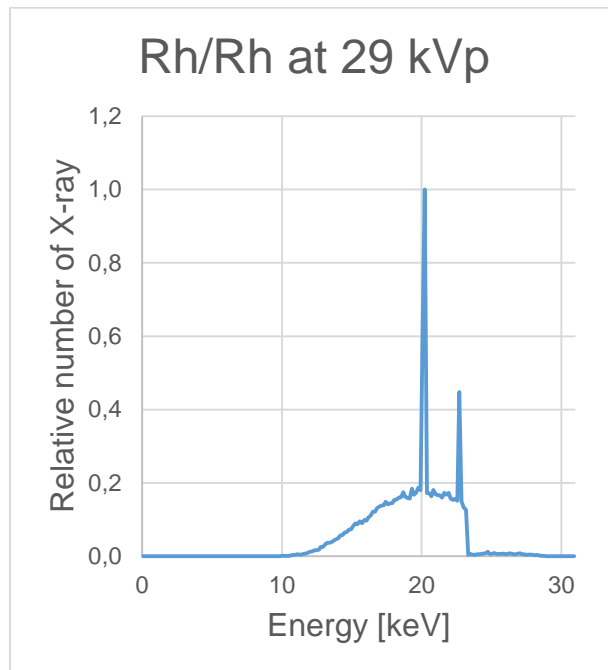


Figure 5-2 Spectral distribution of Rh/Rh at 29 kVp.

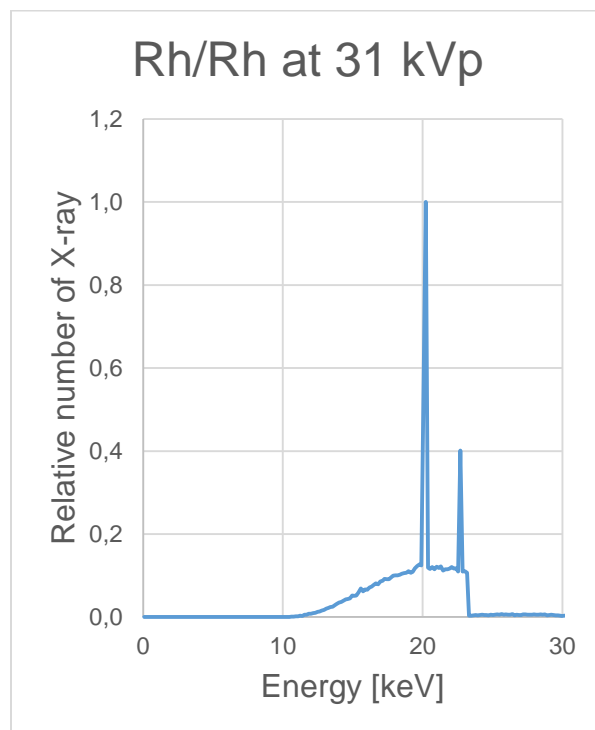


Figure 5-3 Spectral distribution of Rh/Rh at 31 kVp.

Table 5-1 Comparison between characteristics radiation energy of two target/filter combination, including k-shell binding energy of filter effect

	Target effect				Filter effect			Percentage error		
	MC		Literature [36]		MC	Literature	Filter effect			
	Characteristics X-ray	Characteristics X-ray	Characteristics X-ray	Characteristics X-ray	Energy threshold for attenuation beyond K-edge of the target [keV]	Energy [36] threshold for attenuation beyond K-edge of the target [keV]				
	$K_{\alpha}$ [keV]	$K_{\beta}$ [keV]	$K_{\alpha}$ [keV]	$K_{\beta}$ [keV]			$K_{\alpha}$ [keV]	$K_{\beta}$ [keV]		
Mo/Rh at 26 kVp	19.579	17.475	19.600	17.500	23.475	23.220	0.107	0.143	-1.098	
Rh/Rh at 29 kVp	22.730	20.180	22.700	20.200	23.330	23.220	-0.132	0.099	-0.474	
Rh/Rh at 31 kVp	22.707	20.227	22.700	20.200	23.327	23.220	-0.031	-0.134	-0.461	

## 5.2 HVL

Table 5-2 lists the results of *HVL* obtained with the MC simulation and experimentally. Additionally, range of *HVL* values which would be acceptable for a clinical mammogram have been listed

Table 5-2 *HVL* for experimental setup and MC simulations. Acceptable range are obtained from the IAEA 2011 [9] with the equation (5) described in section 2.2.2.

	HVL MC (mmAl)	Experimental HVL (mmAl)	IAEA Acceptable range (mmAl)
<b>Mo/Rh</b> (26kVp)	$0.370 \pm 0.011$	-----	0.290 – 0.450
<b>Rh/Rh</b> (29 kVp)	$0.457 \pm 0.021$	$0.436 \pm 0.026$	0.320 – 0.510
<b>Rh/Rh</b> (31 kVp)	$0.437 \pm 0.012$	-----	0.340 – 0.530

### 5.3 Heel effect

The spectral distribution for five regions of the beam along the x-axis at the detector plane (profile showed in Figure 5-4) are presented in Figure 5-5A. The regions defined in Table 4-8 are displayed in Figure 5-4 between the dashed lines.

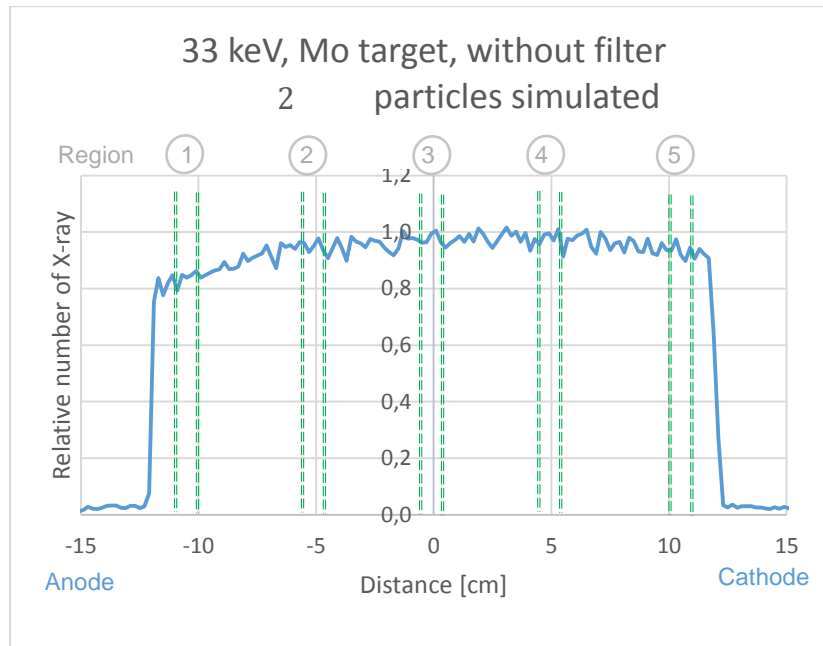


Figure 5-4 Beam profile along X-axis. Dashed areas show the five regions for which spectra were compared.

For a better appreciation of the variation, the region of the peak corresponding to 17.4 keV of the beam, was zoomed in Figure 5-5B.

Table 5-3 lists the photon intensity at each region compared to the central one.

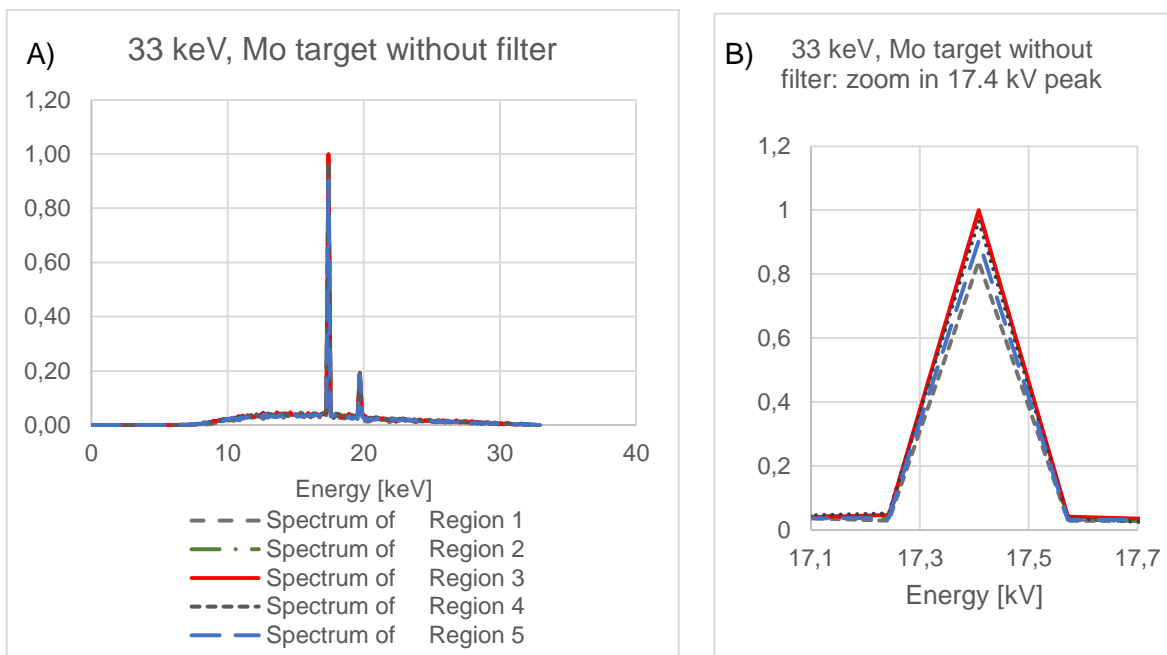


Figure 5-5 Comparison between 5 spectral distribution of the same beam along the x-axis. Figure A shown the spectral distributions and figure B shown 17.4 kV energy peak. Legend figure A is the same as that of B.

Table 5-3 Percentage variation of the different regions with respect to the center

Spectrum of Region 1	Spectrum of Region 2	Spectrum of Region 3	Spectrum of Region 4	Spectrum of Region 5
16.07%	0.37%	0.00%	3.26%	9.61%

The mean energy value of the spectrum in the first and second region varies in a 2% and 1%, respectively with the mean energy value (obtained with the equation (1)) at the central axis. Region 4 and 5 does not have significant variations with respect to the axis.

## 5.4 Kernels

Percentage depth dose deposition kernel (corresponding to the spectra of the central region depicted in Figure 5-1, Figure 5-2 and Figure 5-3) within the detector for the three simulated beam qualities are plotted in Figure 5-6. The kernel shape (of Mo/Rh at 26 keV) at 250  $\mu\text{m}$  depth in detector plane is displayed in Figure 5-7A.

Given the small spectral differences found in the five regions, the same deposition kernel will be used across the detector.

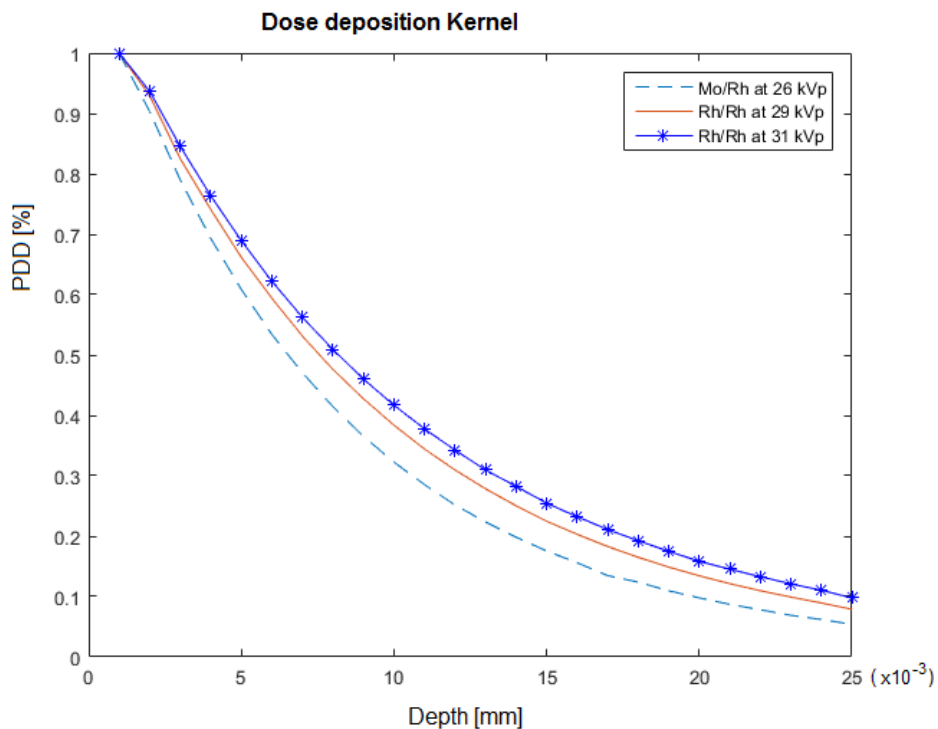


Figure 5-6 Percentage depth dose deposition of the pencil beam within the detector, at the central axis of the beam, for the three simulated beam qualities

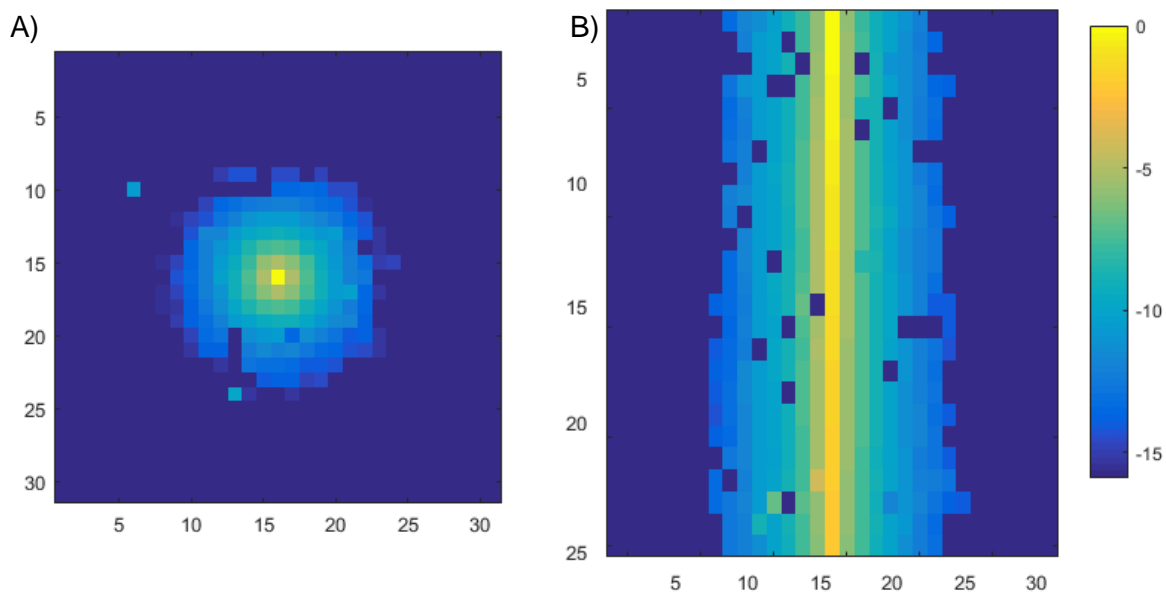


Figure 5-7 A) Kernel shape, 31 x 31 pixel at 250  $\mu\text{m}$  depth in detector plane. Figure B) shown the dose deposition within the detector. Beam quality used for the image was Mo/Rh at 26kVp. Images were taken in logarithmic scale.

## 5.5 Monte Carlo calibration factor

For the experimental measurements, 3 different tube current were used. The MC calibration factors for these values using equation (10) are listed in Table 5-4.

Table 5-4 Entrance dose for experimental data, MC simulations and MC calibration Factor.

	Experimental Data			Monte Carlo Data		$C_{MC}$ [1/ mAs] ( $\times 10^{+08}$ )	$\overline{C_{MC}}$ [1/mAs] ( $\times 10^{+08}$ )
	$TC$ [mAs]	$D_{entrance}^{exp}$ [mGy]	$\frac{N}{TC} D_{entrance}^{exp}$ [mGy] [mAs]	$D_{entrance}^{MC}$ [Gy] ( $\times 10^{-23}$ )	$D_{entrance}^{MC} \times NH$ [mGy] ( $\times 10^{-10}$ )		
Mo/Rh 26kVp	32	2.31	0.072			11.0	
	40	2.85	0.071	3.27	0.65	10.9	$10.90 \times 10^{+08}$ $\pm 9.96 \times 10^{+06}$
	50	3.53	0.071			10.8	
Rh/Rh 29 kVp	50	4.82	0.096			8.23	
	63	6.11	0.097	5.85	1.17	8.28	$8.18 \times 10^{+08}$ $\pm 10.7 \times 10^{+06}$
	71	6.68	0.094			8.04	
Rh/Rh 31 kVp	63	7.92	0.126			8.79	
	71	8.93	0.126	7.15	1.43	8.80	$8.81 \times 10^{+08}$ $\pm 1.68 \times 10^{+06}$
	80	10.1	0.126			8.83	

## 5.6 Detector Calibration factor

The value of the MC output fluences in regions 1 through 5 of

Figure 4-5 were obtained and compared with the gray values from the EPID image (for the same ROIs) of the detector, by equation (15) to obtain calibration detector  $C_{detector}$ . Those values were calculated and are presented in Table 5-5.

Table 5-5 Mean detector calibration factor

	ROI1 ( $\times 10^{+06}$ )		ROI2 ( $\times 10^{+06}$ )		ROI3 ( $\times 10^{+06}$ )		ROI4 ( $\times 10^{+06}$ )		ROI5 ( $\times 10^{+06}$ )		$C_{detector}$ [photons/electrons]
	MC	EXP									
<b>Mo/Rh</b> 26kVp, 40mAs	149	7.9	150	8.0	152	8.1	149	8.0	667	6.6	<b>17.06</b>
<b>Rh/Rh</b> 29 kVp, 63mAs	229	8.9	228	8.9	232	9.0	229	8.9	122	7.7	<b>23.72</b>
<b>Rh/Rh</b> 31 kVp, 71mAs	181	6.0	184	6.1	173	6.1	177	6.1	106	5.4	<b>27.50</b>

## 5.7 Deconvolved output fluence

The kernel dose deposition depends on energy spectrum, X-ray tube current, thickness and material phantom, whose contribution is within the primary fluence value ( $\Phi_{out,(x,y)}$ ) that will impinge on the detector, and, on the other hand, the kernel ( $K_{dep,(x,y,z)}$ ) also depend detector material and how the dose is deposited therein in  $(x, y, z)$  distribution.

The image converted in fluence ( $\Phi_{det,(x,y)}$ ) is a convolution between output fluence of the breast and a kernel that characterized the dose deposition in the detector:

$$\Phi_{det,(x,y)} = \Phi_{out,(x,y)} \otimes K_{dep,(x,y,z)} \quad (15)$$

To obtain the output fluence from the breast from the image, it will work in Fourier Space following these steps:

$$\begin{aligned} \Phi_{det,(x,y)} &= \Phi_{out,(x,y)}^{deconvolved} \otimes K_{dep(x,y)}, \\ \mathcal{F}(\Phi_{det,(x,y)}) &= \mathcal{F}(\Phi_{out,(x,y)}^{deconvolved} \otimes K_{dep(x,y)}), \\ \mathcal{F}(\Phi_{det,(x,y)}) &= \mathcal{F}(\Phi_{out,(x,y)}^{deconvolved}) \cdot \mathcal{F}(K_{dep(x,y)}), \\ \mathcal{F}(\Phi_{out,(x,y)}^{deconvolved}) &= \mathcal{F}(\Phi_{det,(x,y)}) \div \mathcal{F}(K_{dep(x,y)}) \end{aligned} \quad (16)$$

replacing  $\Phi_{det,(x,y)}$  from the equation (14) is obtained:

$$\Phi_{out,(x,y)}^{deconvolved} = \mathcal{F}^{-1} \left[ \frac{\mathcal{F}(C_{detector} \cdot I_{EPID,(x,y)})}{\mathcal{F}(K_{dep(x,y)})} \right] \quad (17)$$

Note that deposition kernel has 3 dimensions but in the next steps a 2D function has been used (shown equation (16)). That is because deconvolution process is in two dimensions, but many times as the z value. Section 5.7.1 will explain that with more details.

The final equation to obtain dose at a certain plane is:

$$D(z) = D_{entrance} \left( \frac{SDD - d}{SDD - d + z_{phantom}} \right)^2 \cdot \frac{\Phi_{in,(x,y)}^{MC}}{\mathcal{F}^{-1} \left[ \frac{\mathcal{F}(C_{detector} \cdot I_{EPID,(x,y)})}{\mathcal{F}(K_{dep(x,y)})} \right]} \cdot 100 \quad (18)$$

### 5.7.1 Deconvolution process in Matlab

After kernel generation, the deconvolution process requires a direct division of two bidimensional matrices after having applied Fast Fourier Transform (*FFT*) in each one, described in equation (17). However, direct division of two matrices requires that they be of equal dimension, but the kernel has the dimensions with which it was simulated in the detector (31,31,25), which is why for each of the kernels, a 3D matrix is created with the same dimensions as the image on the x and y-axis, maintaining the dimension of the z-axis.

In our case, all simulation of the detector was with 25 pixels in z-axis (0.001 *cm* pixel size to complete 0.025 *cm* of thickness)

Note that the kernel along the z-axis ( $z = 1:25$ ) contains dose deposition from the upper face of the detector until the end of it. The deconvolution process must be generated 25 times from the last kernel frame  $K(:, :, 25)$  to the first one  $K(:, :, 1)$  (In matlab the notation  $K(i, :)$  indicates the vector that is in row  $i$ . If the matrix is of 3 dimensions, the notation  $K(:, :, 25)$  corresponds to the 2D matrix that is located in the plane 25)

As we do not want the information of the dose deposition within the detector, but rather the scatter that occurs in it, we must normalize each frame of the kernel by its maximum.

Once the deconvolution is generated, the inverse Fast Fourier Transform ( $FFT^{-1}$ ) (equation (18)) is applied to obtain the output image of the detector, obtaining breast output fluence

Each deconvolution process generates a shift in the resulting image, which is half the size of the dimension-1 ( $(d - 1)/2$ ) of the kernel for each side. To understand this shift, a similarity is made to the associated convolution process.

As shown in Figure 5-8 the kernel corresponds to an operator that produces an average effect in the central pixel, but weights the value of each element with respect to the distance with the central element.

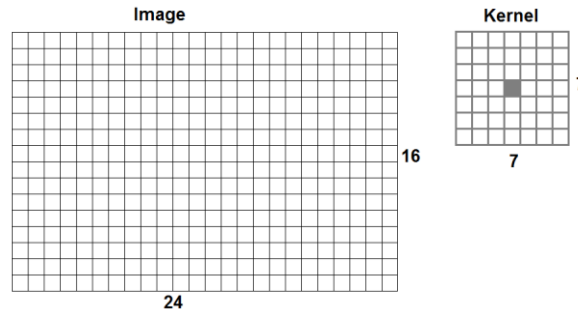


Figure 5-8 Scheme of image and kernel

When applying the convolution of the kernel on the image (in position A), the matrix of  $16 \times 24$  pixels, the value of the first convolution will be positioned at the position of the central pixel of the kernel in the convolution image, as seen in Figure 5-9. However, when the kernel covers the image until it reaches the B position, the central pixel of the image is outside of the image size, and therefore the convolved pixel corresponds to the 22 position of the convolved image. This occurs for both rows and columns.

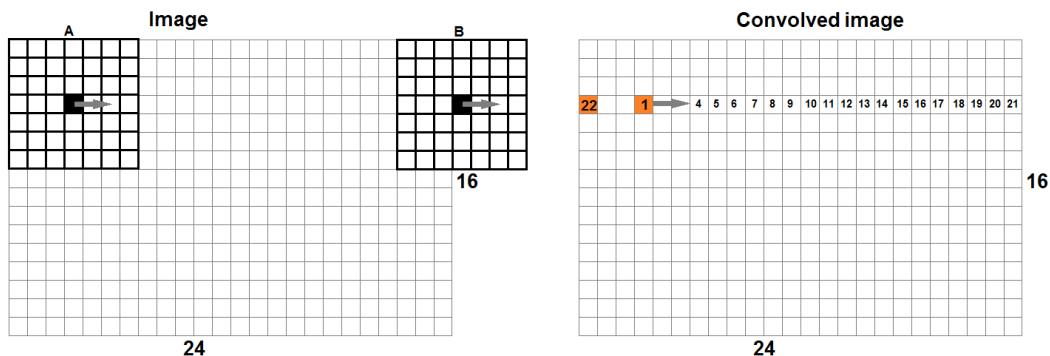


Figure 5-9 Scheme of a convolution process in one row

If the dimension of the kernel is  $7 \times 7$ , such as in the previous example, a shift of  $(7 - 1)/2 = 3$  pixels to the right is produced.

The same issue occurs in the deconvolution process (as seen in Figure 5-10). In our case, as this process is repeated 25 times, the shift is in 375 pixels for an  $31 \times 31$  pixel kernel, up and left. In this case, the program modifies the shift so that the position of the image does not change.

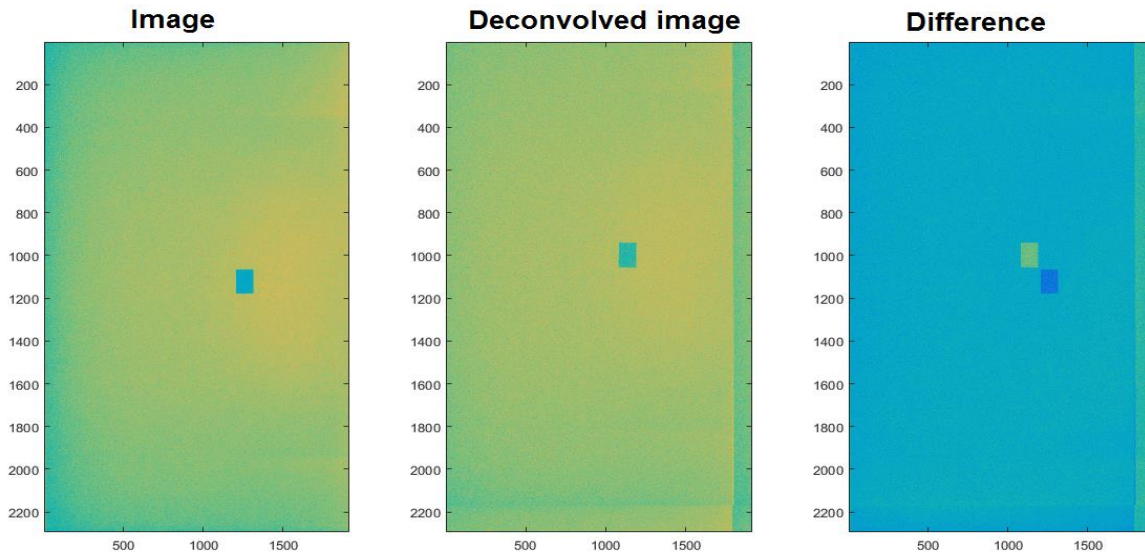


Figure 5-10 Shift in the deconvolution process in a reference image, the third image is pixel to pixel difference between image and deconvolution image

### 5.7.2 Validation of the deconvolution process

A virtual phantom was developed for the validation of the deconvolution algorithm, and 2D Gaussian Smoothing kernel, that convolved a test image, was generated (as display in Figure 5-11). Additionally, on the other hand, the deconvolution mathematical model equation (18) was applied to obtain the original image again as we see in Figure 5-12.

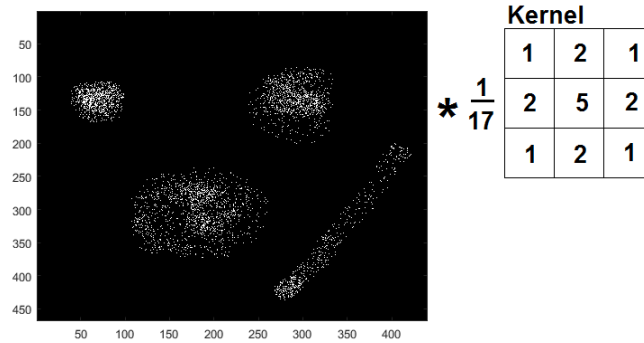


Figure 5-11 Virtual phantom convolved with a blurring kernel

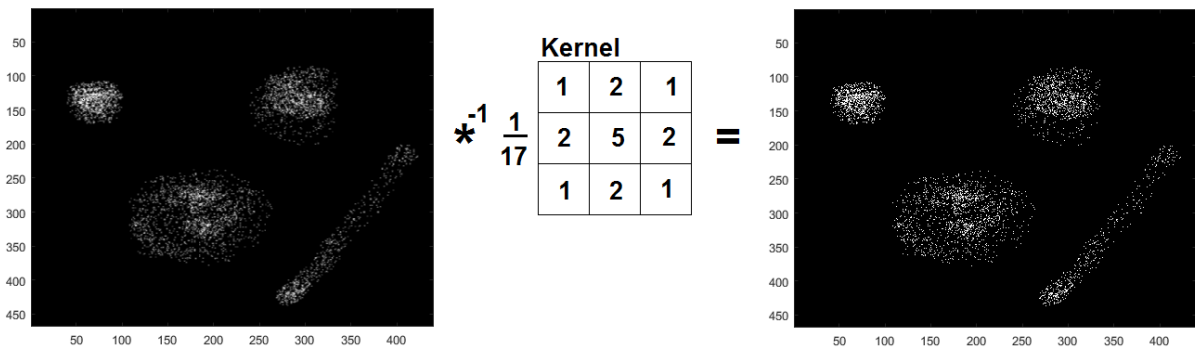


Figure 5-12 Deconvolution process of virtual image

The virtual phantom serves us to obtain the error associated to the deconvolution, since, not knowing the fluency that enters the detector, we can not obtain it, comparing the images that is convoluted with the deconvolved. However, in the process of deconvolution of the virtual phantom, we know the image before the convolution and therefore we can compare the pixel to pixel difference with the deconvolved image.

The error associated for one deconvolution process is:

$$\sigma = \sqrt{\sum_{i,j} (img_{original}(i,j) - img_{deconvolved}(i,j))^2}$$

Obtained  $\sigma = 2.23 \times 10^{-11}\%$  of error in the deconvolution process.

## 5.8 Absorbed dose at a mid-plane of the phantom

Table 5-6 presents the input and output fluence of the three cases, in which the MC input fluence was calibrated by the found factor before. Table 5-7 shown linear attenuation coefficients obtained with the equation (14).

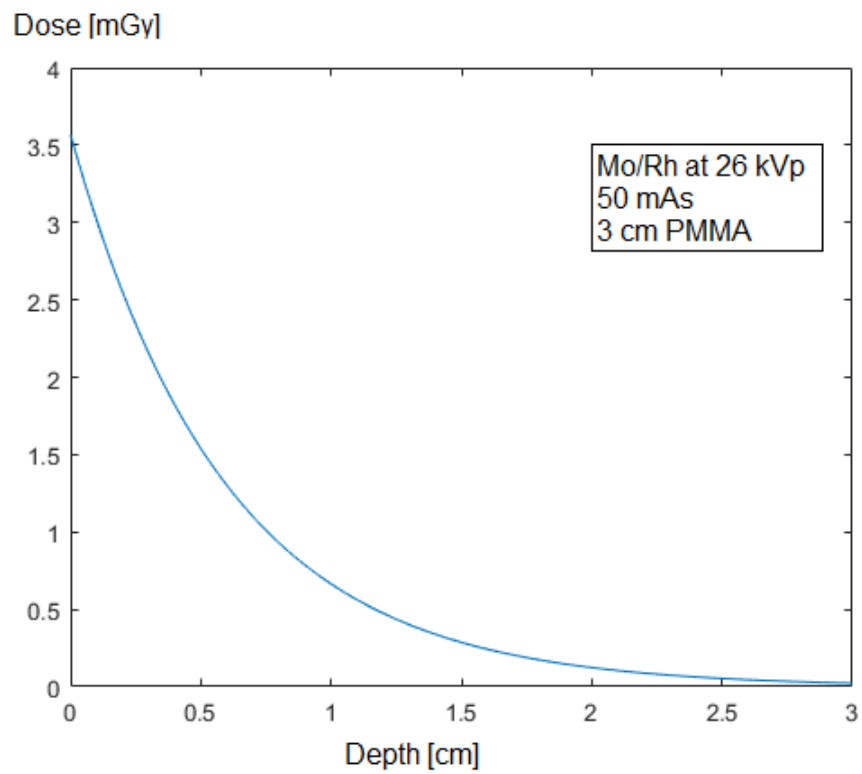
Table 5-6 Number of incident particles into the phantom and number of exit particles of the phantom

	ROI1		ROI2		ROI3		ROI4		ROI5	
	MC input	Output fluence (decon.)								
<b>Mo/Rh</b> 26kVp	1.48E+10	1.40E+08	1.48E+10	1.41E+08	1.90E+10	1.42E+08	2.68E+10	1.41E+08	1.88E+10	1.15E+08
<b>Rh/Rh</b> 29 kVp	4.57E+10	2.10E+08	3.62E+10	2.12E+08	4.74E+10	2.14E+08	3.61E+10	2.12E+08	3.61E+10	1.83E+08
<b>Rh/Rh</b> 31 kVp	9.30E+10	1.66E+08	7.91E+10	1.67E+08	7.85E+10	1.69E+08	7.77E+10	1.68E+08	7.64E+10	1.47E+08

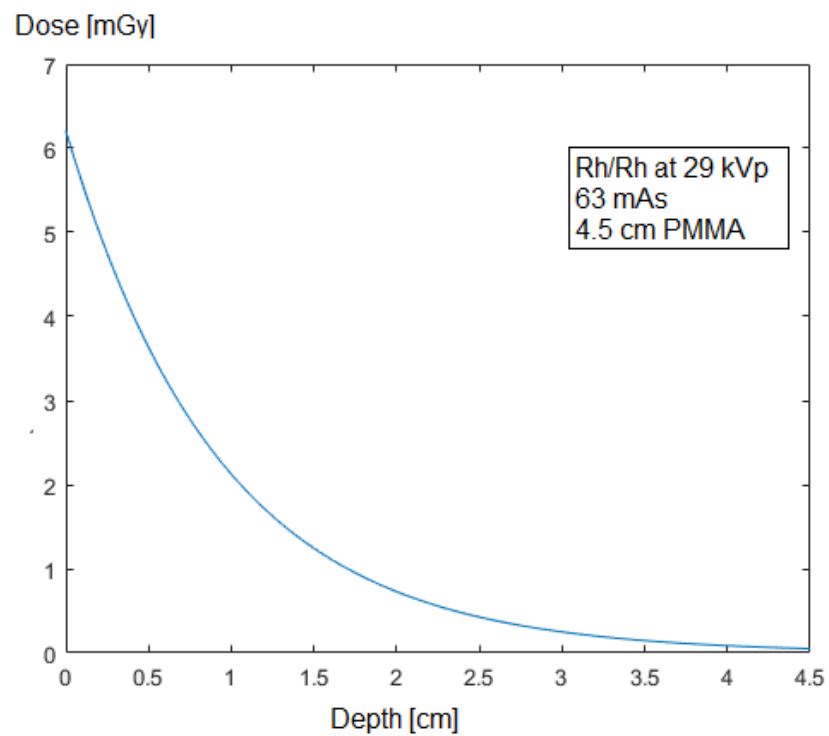
Table 5-7 Linear attenuation coefficient of the phantom from deconvolution process of three combinations target/filter

	$\mu [cm^{-1}]$ <b>PMMA</b>	$\mu/\rho [cm^2/g]$ <b>PMMA</b>
<b>Mo/Rh at 26kVp</b>	<b>1.62</b>	<b>1.37</b>
<b>Rh/Rh at 29 kVp</b>	<b>1.17</b>	<b>0.99</b>
<b>Rh/Rh at 31 kVp</b>	<b>1.03</b>	<b>0.87</b>

A)

**Depth dose within the phantom**

B)

**Depth dose within the phantom**

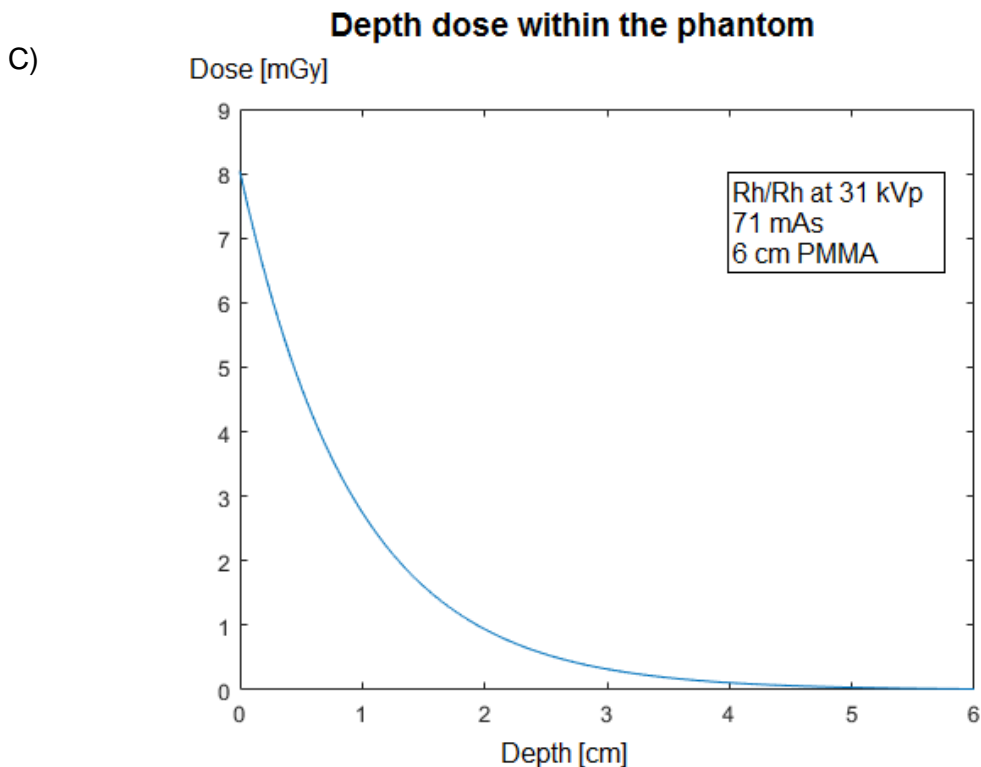


Figure 5-13 Graph of depth dose within the PMMA phantom. A) shown the dose deposition with the mean calibration factor and entrance dose calculated in Table 5-4 case I. B) shown with factors in case II of the same table. and C) depicts depth dose in the case III. Attenuation factors were obtained from Table 5-7 meaning the linear attenuation values for each case.

Figure 5-13 displays the depth dose deposition within the PMMA phantom of the cases previously explained, calculated with the equation (16). Entrance dose used was from the experimental setup. Case A shown Mo/Rh at 26 kVp in 3 cm of PMMA, case B shown Rh/Rh at 29 kVp in 4.5 cm of PMMA, and case C shown Rh/Rh at 31 kVp in 6 cm of PMMA.

## 5.9 Mean Glandular Dose

Beam Quality	Tube Current	PMMA thickness	MTP [C]	HVL	Nk [Gy/C]	g	s	c	MGD [mGy]
Mo/Mo at 26 kVp	32		2.85E-11						<b>0.73</b>
	40	3.0	3.51E-11	0.37	79087509	0.3222	1	1	<b>0.89</b>
	50		4.35E-11						<b>1.11</b>
Mo/Rh at 29 kVp	50		5.68E-11						<b>1.14</b>
	63	4.5	7.21E-11	0.436	78931955	0.25072	1.017	1	<b>1.45</b>
	71		7.87E-11						<b>1.58</b>
Mo/Rh at 31 kVp	63		8.88E-11						<b>1.33</b>
	71	6.0	1E-10	0.437	78929599	0.1868	1.017	1	<b>1.50</b>
	80		1.13E-10						<b>1.70</b>

Using the depth dose deposition showed in Figure 5-13 it is possible to determine the plane at which dose is equivalent to the mean glandular dose (corresponding to each current used for the deconvolved image). Values are list in Table 5-8.

Table 5-8 Thickness of the phantom in which the dose is equivalent to the MGD

Beam Quality	Phantom thickness	Tube current	MGD [mGy]	Thickness from the top of the phantom
Mo/Mo at 26 kVp	30 mm	50 mAs	0.89	0.67 mm
Mo/Rh at 29 kVp	45 mm	63 mAs	1.45	1.19 mm
Mo/Rh at 31 kVp	60 mm	71 mAs	1.50	1.56 mm

## 5.10 Dosimetry tool “BreDose“

An in-house user interphase MATLAB program „*BreDose*“ was developed to get dose at a axial central plane of the mammary gland or the phantom from the deconvolution process, with a MC kernel. BreDose deconvolves the detector image with a specific MC Kernel selected from the reading of the DICOM header. At the same time, the input fluence is selected and entrance dose simulated as an input for equations (13), (11) and (19) to get the dose in a middle level of the breast or phantom.

Through different MATLAB routines, BreDose displays results such as:

- Calibration Factor of Monte Carlo simulation, Detector calibration and entrance dose.
- Displays detector and deconvolved images.
- From the 5 regions of interest (ROIs) defined above, the input fluence to the breast (MC) are compared to the output fluence of this (deconvolved image) and equation (13) is applied to obtain the linear absorption coefficient of the phantom or material between compressor paddle and detector.
- For each linear absorption coefficient, or mean of them, the percentage depth dose within the phantom is plotted and then, weighted by the entrance dose, the user can evaluate the dose in some medium plane of the phantom.

BreDose read the header of DICOM file entered and select relevant information to identify which kernel will be used:

- Size of the image
- Energy
- Exposure
- Anode and filter material

The user must have entered thickness of the phantom and select its material.

Once the program knows that relevant information, it searches the database and select a specific kernel file, input and MC output fluence.

After the deconvolution process, and calculate the calibration factors, BreDose shows the output fluence and linear attenuation coefficient of 5 regions showed in Figure 4-5. Depending on the selection of the user, the program uses one of them (or the average) to obtain the percentage depth dose within the phantom, showing the graph of this.

In this way, and working with equation (18), the dose is obtained at an intermediate level of the breast.

Figure 5-14 shows the user-interface of the BreDose program.

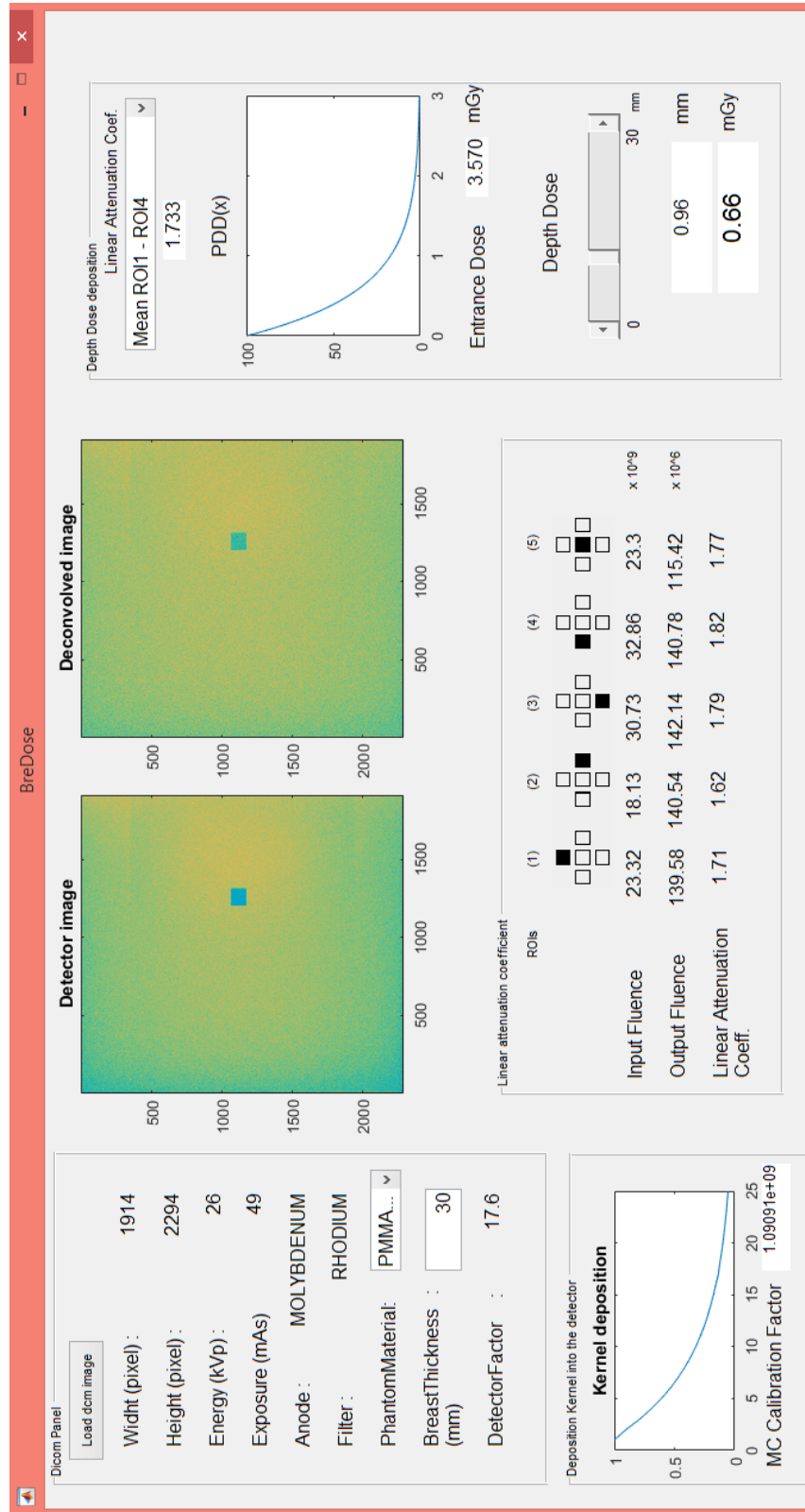


Figure 5-14 User interphase of BreDose

## 6 Discussion

### 6.1 MC validation

The spectral distribution of the MC was performed to verify that the simulation was well done and therefore the characteristics energies of each spectrum were comparable with the literature as well as threshold for attenuation beyond K-edge of the target produced by the filter. Small differences between the simulations results and literature values were obtained ( $< 1.1\%$  in the case of the effect produced by the filter for the Mo/Rh combination). These results suggest that the MC beam simulation is correct.

Another MC validation was carried out by values of HVL values. The HVL value of the experimental setup was compared with MC simulation. Both results were within the range of acceptance tolerance and present a percentage difference of 4.82% for the Rh/Rh at 29 kVp. Unfortunately, no HVL values for the other beam qualities could be experimentally estimated. Nevertheless, values obtained with MC agree with IAEA recommended values for the beam qualities.

In the process of kernels generation, only the spectrum of the central region of the beam was used, although the image is deconvolved throughout all regions in the field. In order to evaluate if it is possible to use a common spectrum for the process, it was necessary to know the spectral behaviour of the beam at different points. It was studied 5 regions along the x-axis where the heel effect occurs since it is known that there is a percentage difference of intensity along the axis. Difference between those spectra was analysed and it was observed that, as expected, there is no difference across the range of energies since there is no other filtration in another sector of the beam. Only the beam intensity varies, which will have an effect within the detector calibration factor discussed in section 5.6. This part of the

research suggests that it is possible use a single kernel for each configuration (i.e. beam quality) and it is not necessary to have another database of kernels for each beam quality. The intensity of the spectrum varies with respect to the central region by up to 16% at the edges as shown in Table 5-3.

After the validation of the Monte Carlo, it was proceeded to generate the kernels, whose combinations were three: Mo/Rh at 26keV, Rh/Rh at 29 keV and Rh/Rh at 31 kVp.

## 6.2 Kernel generation

Kernel deposition can be seen in Figure 5-6 and Figure 5-7. Those depict propagation of this in depth and at the plane of the image. In Figure 5-7 it can be observed that the statistic of this kernel is low since the distribution is not homogeneous, with “empty” pixels. It is necessary to regenerate these kernels simulating a greater number of histories than now ( $2 \times 10^7$ ) for which is estimated calculation time of 8.7 hours (each beam quality).

## 6.3 MC calibration Factor

Monte Carlo calibration factor was obtained comparing the experimental entrance dose with MC entrance dose using the equation (10). Each value was normalized by the tube current value to obtain a normalized calibration factor for each beam quality. Table 5-4 presents the mean value of MC calibration factor, 10.9 [1/mAs] for Mo/Rh at 26 kVp, 8.18 [1/mAs] for Rh/Rh at 29kVp and 8.81 [1/mAs] for Rh/Rh at 31 kVp. In principle, the Rh/Rh combination has a similar value, moreover, it is not possible conclude the behaviour of this factor due to the lack of measurements and simulations.

## 6.4 Detector calibration Factor

By analysing the output fluence of the MC detector with the EPID image, the detector calibration factors were obtained for the three cases and are presented in Table 5-5. Each value obtained with MC is multiplying by its one MC calibration factor and tube current respectively.

These values are those that represent the electron conversion (or signal detected by the complete detection system, either CsI, a-Se and then TFT) to photon fluence. Once the image is converted into fluence, the deconvolution process is applied.

As Table 5-5 shows, the detector calibration factor is around 20 photons per electron generated in a-Se and detected by the TFT in general. Again, it is not possible to appreciate the behaviour of this factor due to the number of measurements used in this work.

## 6.5 Deconvolution

Following the back-projection process, the linear attenuation coefficient were obtained in the three cases, each one were performed comparing only the first four regions of interest to obtain the linear attenuation coefficient of the PMMA without Al layer. These values are in the range of the values presented in the literature for low energies showed in Table 2-2, moreover, they are near to values from a beam energy of 15 keV. It is important to note that the table is described for a monoenergetic beam, not just as experimentally and computationally as this work.

In Figure 5-13 A, B and C the attenuation of dose deposition is seen through the phantom.

Starting on the information in the Table 5-8, it can be concluded that the mean glandular dose is equivalent to that calculated at one-third of the phantom depth (approximately).

---

## 6.6 Future work

As a future work, it is expected to study the behaviour of both calibration factor, specially the detector calibration factor along the x-axis where the heel effect occurs, since it is known that there is a percentage change in the number of photons that impinge on the detector.

Generation of kernel of dose deposition for other configurations and recalculate the ones in this study with a larger number of histories.

The fluences that were compared throughout the work were obtained from 5 regions of interest that are defined by the programmer, however they are defined so that, in the future, the user can move about the image and be able to analyse different regions of the breast. The main problem with this is that the database must contain the input fluence information in all regions of the breast and the Beamdp program does not allow the direct retrieval of it but the user must define specific regions of interest. since either along the x-axis along the y-axis.

It is proposed to use a film dosimetry on the detector and under this, to compare the output fluence of the simulated phantom with the experimental one, and thus to have a better estimate than the one made in this work, where the fluence that was compared was made by interacting the beam with an ideal detector.

On the other hand, it would be interesting to relate the linear absorption coefficient with the glandularity of the breast and from that relation obtain a mean glandular dose for each patient

Finally, it is proposed a systematic validation comparing the MGD of the mammograph with this model for other beam qualities.

## Appendix A

### List of Abbreviations and Acronyms

$\Phi$	Total number of photons
$\bar{E}$	Mean Energy of the spectrum
$\Phi(E)$	Photons Fluence $\Phi$ with energies between 0 and $E$
$\Psi$	Energy Fluence
$\mu$	Linear attenuation coefficients
$HVL$	Half Value Layer
$MGD$	Mean Glandular Dose
PHSP	Phase Space
$C_{MC}$	Monte Carlo calibration factor
${}_{TC}D_{entrance}^{exp}$	Experimental entrance dose for each tube current $TC$
${}_{TC}^N D_{entrance}^{exp}$	Experimental entrance dose for each tube current value normalized by this
$TC_i^{exp}$	Tube current value. for each measure $i$
$D_{entrance}^{MC}$	Monte Carlo absorbed dose at the surface of the phantom
$NH$	Number of histories
${}^{NH}D_{entrance}^{MC}$	Monte Carlo entrance per number of histories
$PDD(z_{phantom})$	Percentage depth dose
$SSD$	Source-surface distance
$\bar{\mu}_M$	Mean value of the linear attenuation coefficient of the medium $M$
$\Phi_{in.(x,y)}$	Incident fluence of particles from the phantom
$\Phi_{out.(x,y)}$	Output fluence of particles from the phantom
$I_{EPID.(x,y)}$	Gray values of the EPID image
$I_{EPID}^{ROI_i}$	Gray values of region $i$ from EPID image
$\Phi_{det. (x,y)}$	Output fluence of particles from the detector
$C_{detector}$	Detector calibration factor
$N_{MC}^{ROI_i}$	number of counts for region $i$ from MC simulation
$K_{dep.(x,y,z)}$	Kernel deposition within the detector

## Bibliography

- [1] “Susan G Komen,” [Online]. Available: <http://ww5.komen.org/breastcancer/earlydetectionampscreening.html>. [Accessed 2016].
- [2] G J Heyes, A J Mill and M WCharles, “Mammography—oncogenecity at low doses,” *Journal of Radiological Protection*, vol. 29, p. A123–A132, 2009.
- [3] J. T. Bushberg, et al., *The Essential Physics of Medical Imaging.*, Lippincott Williams & Wilkins, 2011.
- [4] M. J. Yaffe, “Mammographic density. Measurement of mammographic density,” *BioMed Central: Breast Cancer Research*, Toronto, Ontario, Canada, 2008.
- [5] AIEA, “AIEA Radiation Protection of Patients,” International Atomic Energy Agency, 2013. [Online]. Available: [https://rpop.iaea.org/RPOP/RPoP/Content-es/InformationFor/HealthProfessionals/1\\_Radiology/Mammography/mammography-technique.htm#MFAQ04](https://rpop.iaea.org/RPOP/RPoP/Content-es/InformationFor/HealthProfessionals/1_Radiology/Mammography/mammography-technique.htm#MFAQ04).
- [6] P. Mayles, et al., *Handbook of Radiotherapy Physics: Theory and Practice*, Taylor & Francis, 2008.
- [7] Daniel B Kopans MD,, *Breast Imaging*, Lippincot Williams & Wilkins, 2006.
- [8] S. Kettner, et al., “Reduction of radiation doses to adolescents undergoing scoliosis x-ray imaging,” *European Society of Radiology*, Rambam Medical Center, Haifa, Israel.

- 
- [9] I. A. E. A. IAEA, "Quality Assurance Programme for Digital Mammography.," in *IAEA human health series N17*, Vienna, Austria, 2011.
- [10] F. H. Attix, *Introduction to Radiological Physics and Radiation Dosimetry*, John Wiley & Sons, 1986.
- [11] N. I. o. S. a. Commerce, "NIST," [Online]. Available: <http://physics.nist.gov/PhysRefData/XrayMassCoef/tab4.html>.
- [12] M. J. Yaffe, "Detectors for Digital Mammography," in *Digital Mammography*, Springer, 2010, pp. 13-31.
- [13] R. Torres Cabrera, "Mamografía Digital: Estado actual de la tecnología," *Elsevier*, p. 7, 24 March 2010.
- [14] A. Todd-Pokropek, "<http://www.pediatricrad.info/w3/>," 2016. [Online]. Available: <http://www.pediatricrad.info/wo/europacs98/abstracts/055.htm>.
- [15] Ernest K.J. Pauwels, et al., "Breast Cancer Induced by X-Ray Mammography Screening? A Review Based on Recent Understanding of Low-Dose Radiobiology," *Medical Principles and Practice* 25(2), pp. 101-109, 2016.
- [16] D. R. Dance, et al., "Estimation of mean glandular dose for breast tomosynthesis: factors for use with the UK, European and IAEA breast dosimetry protocols," *Physics in Medicine and Biology*, vol. 56, p. 453–471, 2011.
- [17] D.R. Dance, "Monte Carlo calculation of conversion factors for the estimation of mean glandular breast dose.," *Physics in Medicine Biology*, vol. 35, no. 9, pp. 1211-1219, 1990.

- [18] D. R. Dance, et al., "Additional factors for the estimation of mean glandular breast dose using the UK mammography dosimetry protocol.," *Physics in Medicine Biology*, vol. 45, no. 11, pp. 3225-3240, 2000.
- [19] D. R. Dance, et al., "Further factors for the estimation of mean glandular dose using the United Kingdom, European and IAEA breast dosimetry protocols.," *Physics in Medicine Biology*, vol. 54, no. 14, pp. 4361-4372, 2009.
- [20] Markus Wendling, et al., "Accurate two-dimensional IMRT verification using a back-projection EPID dosimetry method," *Medical Physics* 33, pp. 259-273, 2006.
- [21] B. Warkentin, et al., "Dosimetric IMRT verification with a flat-panel EPID," *Medical Physics*, Vol. 30, No. 12, vol. 30, no. 12, pp. 3143 - 3155, 2003.
- [22] J Bonsall, T Akram, R Tsang, V Jones, A Turnbull, E Cornford, "Practical evaluation of GE Healthcare SenoClaire digital breast tomosynthesis system," Public Health England, Wellington, London, 2016.
- [23] G. Chorbajian, "Thermoluminescence dosimetry and mean glandular dose estimation in digital breast tomosynthesis," Santiago, Chile, 2015.
- [24] C.-M. Ma, et al., "AAPM protocol for 40–300 kV x-ray beam dosimetry in radiotherapy and radiobiology," *Medical Physics*, vol. 28, no. 6, pp. 868 - 893, 2001.
- [25] R. J. Aukett, et al., "Addendum to the IPEMB code of practice for the determination of absorbed dose for x-rays below 300 kV generating potential (0.035 mm Al–4 mm Cu HVL)," *Physics in Medicine and Biology*, vol. 50, p. 2739–2748, 2005.

- [26] I. Kawrakow, et al., "The EGSnrc Code System: Monte Carlo Simulation of Electron and Photon Transport," NRCC Report PIRS-701, Ottawa, Canada, 2016.
- [27] D.W.O. Rogers, et al., "BEAMnrc Users Manual," NRCC Report, Ottawa, 2016.
- [28] B. Walters, et al., "DOSXYZnrc Users Manual PIRS-794revB," NRCC Report, 2016.
- [29] C. Ghetti, et al., "Physical characteristics of GE Senographe Essential and DS digital mammography detectors," *Medical Physics*, vol. 35, no. 2, pp. 456-463, 2008.
- [30] Stefano Rivetti, et al., "Physical and psychophysical characterization of a novel clinical system for digital mammography," *Medical Physics*, vol. 36, no. 11, pp. 5139-5148, 2009.
- [31] M. O. Díaz, "Scattered radiation in projection X-ray mammography and digital breast tomosynthesis," Guildford, 2013.
- [32] J.Boone, V.Cooper III, "Scatter/primary in mammography: Monte Carlo validation," *Medical Physics* 27, pp. 1818-1831, 2000.
- [33] I. Sechopoulos, et al., "Scatter radiation in digital tomosynthesis of the breast," *Medical Physics*, p. 564–576, 2007.
- [34] Abdelkader Toutaoui, Nadia Khelassi-Toutaoui, Zakia Brahimi, and Ahmed Chafik Chami, "Effects of energy spectrum on dose distribution calculations for high energy electron beams," *Journal of Medical Physics*, 2009.
- [35] Rogers, et al., "BEAMDP Users Manual," NRCC Report PIRS-0509(C)revA, Ottawa, 2016.

- 
- [36] P. Sprawls, "Mammography Physics and Technology," [Online]. Available: <http://www.sprawls.org/resources/MAMMO/module.htm>.
- [37] "National Research Council Canada," [Online]. Available: [http://www.nrc-cnrc.gc.ca/eng/solutions/advisory/egsnrc\\_index.html](http://www.nrc-cnrc.gc.ca/eng/solutions/advisory/egsnrc_index.html).
- [38] "<http://ww5.komen.org/breastcancer/earlydetectionampscreening.html>," [Online].
- [39] [Online]. Available: <http://www.keyword-suggestions.com/cGVyc29uYWwgY28gZGV0ZWN0b3I/>.
- [40] M. Zeidan, "Assessment of Mean Glandular Dose in Mammography," 2009.
- [41] Wendling, et al., "Accurate two-dimensional IMRT verification using a back-projection EPID dosimetry," *Medical Physics*, vol. 33, no. 2, pp. 259-273, Febrero, 2006.
- [42] D. R. Dance, et al., "Average glandular dose in digital mammography and digital breast tomosynthesis: comparison of phantom and patient data," *Physics in Medicine & Biology*, vol. 60, p. 7893–7907, 2015.
- [43] D. R. Dance, et al., "Breast dosimetry," *Appl Radiat Isot.* 50, p. 185–203, 1999.
- [44] J.C. Santos, et al., "Estimation of dose distributions in mammography into a tissue equivalent phantom," January 2015. [Online]. Available: [https://www.researchgate.net/publication/283837656\\_Estimation\\_of\\_dose\\_distributions\\_in\\_mammography\\_into\\_a\\_tissue\\_equivalent\\_phantom](https://www.researchgate.net/publication/283837656_Estimation_of_dose_distributions_in_mammography_into_a_tissue_equivalent_phantom).
- [45] Shih-Ying Huang, et al., "The effect of skin thickness determined using breast CT on mammographic dosimetry 35," *Medical Physics*, pp. 1199 - 1206, 2008 (35).

- [46] John M. Boone and Virgil N. Cooper III, "Scatter/primary in mammography: Monte Carlo validation," *Medical Physics*, vol. 27, no. 8, pp. 1817-1831, 2000.